



**GEOLOGICAL SURVEY OF CANADA  
OPEN FILE 7007**

**Geology and mineralization of the link between  
Hope Bay and Elu Greenstone Belts,  
northeast Slave Craton, Nunavut**

**H. Mvondo, D. Lentz, M Bardoux, D.T. James**

**2012**



Natural Resources  
Canada

Ressources naturelles  
Canada

**Canada**



## **GEOLOGICAL SURVEY OF CANADA OPEN FILE 7007**

# **Geology and mineralization of the link between Hope Bay and Elu Greenstone Belts, northeast Slave Craton, Nunavut**

**H. Mvondo<sup>1</sup>, D. Lentz<sup>1</sup>, M. Bardoux<sup>2</sup>, D.T. James<sup>3</sup>**

<sup>1</sup>Department of Geology, University of New Brunswick, Fredericton,  
NB, Canada

<sup>2</sup>Newmont Mining Corporation, Vancouver, BC, Canada

<sup>3</sup>Canada-Nunavut Geoscience Office, Iqaluit, NU, Canada

**2012**

©Her Majesty the Queen in Right of Canada 2012

doi:10.4095/289889

This publication is available from the Geological Survey of Canada Bookstore  
([http://gsc.nrcan.gc.ca/bookstore\\_e.php](http://gsc.nrcan.gc.ca/bookstore_e.php)).

It can also be downloaded free of charge from GeoPub (<http://geopub.nrcan.gc.ca/>).

### **Recommended citation:**

Mvondo, H., Lentz, D., Bardoux, M., and James, D.T., 2012. Geology and mineralization of the link between Hope Bay and Elu Greenstone Belts, northeast Slave Craton, Nunavut; Geological Survey of Canada, Open File 7007, 58 p. doi:10.4095/289889

Publications in this series have not been edited; they are released as submitted by the author.



## **ABSTRACT**

Located in the NE Bathurst Block of the Slave Craton, the Hope Bay and Elu belts are two Neoproterozoic greenstone belts striking N-S and NE-SW, respectively. The Elu Belt (EB) southern end is deflected westwards to form a concave connection termed the Elu Link (EL) where 2716 to 2663 Ma supracrustals are in part shared with the adjacent Hope Bay Belt (HBB). The EL supracrustal sequence consists mainly of tholeiitic pillowed metabasalts with lesser amounts of interleaved metadacite, metarhyolite, iron formation, and metashale, having variably recorded  $D_1 - D_3$  deformation. Supracrustals appear to be seamlessly in contact with syn- $D_1$  migmatite orthogneiss on the EL eastern margin. Orthogneiss and supracrustal rocks were both intruded by syn- to late- $D_2$  metagabbros and metagranites. Like in the HBB, Archean magmatic rocks of the EL originated from deep and upper mantle sources in a probable back-arc setting. Sparse NE-striking Proterozoic dolerite dikes derived from deep mantle sources cut the entire rock mass.  $D_1$  deformation was successively accompanied by hydrothermal alteration and prograde metamorphism reaching epidote-amphibolite facies peak conditions, but related structures are strongly obscured by  $D_2 + D_3$  overprint.  $D_2$  that initiated under prograde metamorphism and was further accompanied by greenschist retrogression deformed  $D_1$  fabrics around tight to open curvilinear  $F_2$  folds forming a foliation triple junction between the EB + HBB. The  $F_2$  folds together with  $L_2$  radial stretching lineation and coeval shear zones show that the EL is rimmed around a syn-compression large-scale  $D_2$  dome.  $D_3$  is a brittle-ductile deformation lacking any visible fabric. Both  $D_2 + D_3$  denote vertical general flattening dominated transpression with E-W maximum compression and N-S minimum extension. They illustrate asymmetric syn-compression exhumation of the HBB and EB that were further affected by strain-free greenschist retrogression due to the Thelon Orogeny. The mineralization comprising Au-As-Cu-Zn metals in most EL rock units occurred prior and, possibly, during metamorphism, was further remobilized by subsequent tectonic and thermal events. It follows that ore mineralization occurrence in the EL is chiefly lithologically and structurally controlled.

## SUMMARY

### *Geology*

The EL comprises 6 units in inferred chronological order; 1) Metavolcanic-minor metasedimentary supracrustals (metapsammite + iron formation); 2) Migmatitic orthogneiss; 3) Metagabbro; 4) Porphyritic metagranite; 5) Equigranular metagranite; and 6) Dolerite-anorthosite-pegmatite dikes.

Stratigraphic relationships and volcanic cycles have not been defined to date due to intensive strain overprint and cross-cutting plutonism. As such, the EL mafic metavolcanic rocks resemble the iron tholeiitic basalts mapped on the eastern side of the HBB. The occurrence of metapsammite and iron formation within the EL may be indicative of multiple volcanic cycles in the belt.

The mafic metavolcanic rocks and related interbeds depict three metamorphic assemblages ( $M_1$ - $M_3$ ) interpreted as; 1) prograde metamorphic overprint of a pre-existing hydrothermal mineral assemblage accompanying the regional deformation and reaching peak conditions in the epidote-amphibolite facies, 2) greenschist retrograde metamorphism accompanying the regional deformation, and 3) post-tectonic greenschist retrograde metamorphism. Migmatization on the eastern side of the EL is thought to reflect high-grade regional metamorphic conditions during and after which most felsic magmatic bodies were emplaced towards structurally higher levels. NE-trending dolerite dikes are late- to post-tectonic intrusions, which, together with their hosts, recorded Proterozoic greenschist facies static recrystallization.

The EL mafic metavolcanic rocks and associated mafic intrusions range in composition from subalkaline basaltic to andesitic. On a  $TiO_2$ - $Al_2O_3$  diagram, the EL mafic metavolcanic rocks plot across 3 boundaries that are delineating so-called A-C suites that are currently defined at specific ratios in the HBB. Under the same principles, EL metagabbros plot in the B + C fields. Both the mafic metavolcanic and metaplutonic rocks of the EL are further divided into four sub-suites characterized by; 1) Ti + LREE enriched rocks, 2) Ti-enriched flat REE rocks, 3) Ti-depleted LREE-enriched rocks, and 4) Ti-depleted flat REE rocks, all inferred to have derived from deep and upper mantle sources. The felsic metavolcanic rocks are dacitic to rhyolitic lavas, whereas felsic intrusives range in composition from granodiorites to granites. Felsic rocks are inferred to represent the most fractionated magmas in the area. Younger dolerite and anorthosite dikes define a Ti+LREE enriched suite derived from a deep mantle source. Both the mafic and felsic rocks of the EL indicate a back-arc tectonic setting of emplacement.

Supracrustals and migmatitic orthogneiss exhibit two main fabric-forming deformation events ( $D_1 + D_2$ ), whereas the metagabbros and related metagranites only recorded  $D_2$  deformation.  $D_1$  is a poorly preserved deformation event inferred to originate from horizontal compression that was

successively accompanied by hydrothermal alteration and prograde metamorphism leading to partial melting and emplacement of granitic rocks cropping out in the eastern margin of the EB. D<sub>2</sub> deformation pervasively affects intrusive rocks and their supracrustal hosts and corresponds to a vertical general flattening dominated transpression with maximum E-W compression and intermediate N-S extension. This deformation event was partly accompanied by prograde metamorphism with epidote-amphibolite facies peak conditions and migmatization before reversal into greenschist regression. It resulted in the asymmetrical exhumation of the EB as compared to the neighbouring HBB. A curved reverse shear zone (the OPIK Shear Zone), bounding the EL to the north and inferred to extend along the eastern margin of the HBB is due to formation of a D<sub>2</sub> compressional dome, centered about the Angimajuk Metagranitoid Complex (AMC) between the HBB and EB. D<sub>1</sub>-related foliation folded around tight to open curvilinear F<sub>2</sub> folds on the edge of the AMC forms a foliation triple junction (basin structure) between the HBB and the EL. A third brittle-ductile deformation event D<sub>3</sub> having the same finite strain geometry as D<sub>2</sub> but lacking any visible fabric is also recorded in the two belts.

### ***Alteration and mineralization***

The area of interest straddles two alteration styles. Most rock types therein exhibit chloritization, sericitization, and epidotization, but many rock units also show variably intensive silicification and hematization. Pervasive ankerite-chlorite alteration typical of the HBB is mainly observed west of the Four Lakes area. Alteration assemblages generally follow D<sub>2</sub> structures including shear zones, microlithons, tension gashes, fold closures, and boudin necks. East of Four Lakes, alteration is primarily characterized by pervasive epidotization and silicification.

No visible gold has been observed in the field. However, anomalous concentrations of As + Au + Cu + Zn are present in most EL rock units. Textural and microstructural evidence suggests that as many as 3 base-metal sulfide phases formed during M<sub>1</sub> to M<sub>3</sub> metamorphic stages. Though there is insufficient field evidence yet to demonstrate a continuum, it is suggested that metal endowment that may have formed perhaps as soon as ca. 2716 Ma volcanism was further amplified by the emplacement of syn-tectonic metagabbros and continuously remobilized during subsequent tectonometamorphic events. D<sub>2</sub> structures defining the last fabric-forming deformation event were used as the main fluid conduits and mineralization traps. Thus, the mineralization in the mapped area appears as lithologically and structurally controlled.

### ***Future work***

This study of the EL shows that the HBB + EB are structurally and lithologically connected. It suggests that the two belts recorded similar geological histories and that mineralization of the HBB may extend into the EL. Hence, extending this extrapolation to the rest of the EB is recommended to help evaluating the economic potential of the entire belt. The migmatitic orthogneiss that borders the eastern margin of the EB requires detailed studies in order to establish the relationship between the gneiss and nearby supracrustal rocks and better constrain the timing of volcanism and the tectonometamorphic history in the two belts. The evolution of the metallogenic environments between these different crustal levels is also of prime interest to the industry. Archean and Proterozoic tectonic overprints in the studied area should be further tested and demonstrated as it may link to potential metal endowment. Detailed mapping starting from the Thelon front located few kilometers east of the EB would help breaking down these tectonic events. Combining this mapping with a tectonometamorphic history derived from age dating (e.g.,  $^{40}\text{Ar}$ - $^{39}\text{Ar}$ ) would complete the study in its precise time frame.

Measurement of magnetic susceptibility data on hand samples of the main rock units in the EL yielded highly contrasting values indicating the presence of rock sub-units. Hence, we recommend a high-resolution magnetic mapping as a powerful tool for mapping the structures and the lithologies in the EB. Because of their Au + As + Cu + Zn anomalous values in the EL, the metagabbros are recommended that they should be given primary attention in terms of mineralization potential. Most felsic metagranitoids are coeval with or postdate the metagabbros and recorded greenschist retrogression. They yield anomalous Au + As + Cu + Zn values that deserves more attention in terms of their deformation history and economic potential. Fluid inclusions and S- O- H isotope investigation, as well as quartz trace element analysis in the belt should be performed to help accounting for the source(s) of the mineralizing fluids and the petrogenetic processes that controlled their transportation and distribution.

## **INTRODUCTION**

Located in the NE corner (Bathurst Block) of the Slave Craton, the Hope Bay Belt (HBB) and Elu Belt (EB) are two adjacent Neoproterozoic greenstone belts striking N and NE, respectively (Fig. 1). The EB is bent westwards in the south to form an arcuate northwards concave E-W connection zone, termed the Elu Link (EL), with the neighbouring HBB (Fig. 1). Both the HBB + EB are located between the Thelon and Wopmay Proterozoic orogens suggesting tectonometamorphic overprint of Archean geological features. Unlike the EB, the HBB has been the focus of several mapping and exploration

projects that resulted in the discovery of major gold deposits including Doris, Boston, and Madrid. Despite this previous work, many key regional scale geological questions remain unanswered. In particular, the tectonic and metamorphic evolution, as well as the mineralization history of the belts is still not well understood. The distinction between Archean and Proterozoic tectonometamorphic and mineralization imprints is not clear. Also, it is not clear if the HBB and EB recorded the same geological history or if they could correspond to different, juxtaposed greenstone belts. This project aims to address this lack of information by documenting major relationships between the two belts. In this contribution, we present a new geological map and cross-sections of the link between the HBB and EB. New structural, petrographic, and geochemical data are also presented. The tectonometamorphic history and the mineralization model of the belt are discussed. Most of our data are compared to those from the Flake Lake area representing the closest segment of the HBB. We propose that the studied area is part of an ancient back-arc basin that suffered multiple ductile deformation phases with the last two representing a syn-compression exhumation that occurred asymmetrically with respect to the HBB and favored mineralization of the two belts.

## **REGIONAL FRAMEWORK**

The NE corner of the Bathurst Block (BB) consists of more than 60% granitoid rocks (Thompson, 1997) occurring with heterogeneous granitoid orthogneiss and metavolcanic rocks represented in part by the HBB and EB. In the southern part of the BB, the granitoids are associated with sedimentary rocks, pink gneiss, and migmatites (Gebert, 1990a; 1993).

The HBB is composed of greenschist to lower amphibolite grade, thick mafic pillowed flows and subordinate metasedimentary rocks, felsic volcanic to volcanoclastic rock intercalations, and syn- to late-volcanic ultramafic intrusions bounded or cut by low- to medium-grade felsic granitoid rocks (e.g., Gebert, 1993; Sherlock, 2004 and references therein). Uranium-lead zircon ages determined by Bevier and Gebert (1991), Hebel (1999), and Shannon (2008) suggest that the HBB supracrustal rocks were deposited between ca. 2716 - 2663 Ma with the minimum age of felsic volcanism dated at ca. 2653 Ma (Bevier and Gebert, 1991). Like the pegmatite dated at ca. 1880 Ma in its northeastern margin (Bevier and Gebert, 1991), Neoproterozoic dolerites cutting the HBB may be related to the Thelon tectonic front located few tens of kilometers east of the EB (van Breemen et al. 1987). The entire Archean assemblage suffered D<sub>1</sub>-D<sub>3</sub> deformation accompanied by a regional metamorphism to greenschist facies and locally amphibolite facies (Thompson, 1997) with a proposed culmination minimum age of 2608 ± 5 Ma obtained by U-Pb on zircons (Bevier and Gebert, 1991). A steep S<sub>0</sub>/S<sub>1</sub> foliation tightly to isoclinally folded by F<sub>2</sub> folds including synformal anticlines (Boston

deposit), and F<sub>3</sub> belt-scale flexures are the main strain features that are further cut by numerous D<sub>4</sub> brittle faults (e.g., Carpenter et al., 2003; Sherlock et al., 2003; 2004).

Gold mineralization in the HBB is commonly associated with quartz and quartz-ankerite-sericite veins occurring throughout the belt regardless of any specific lithology although the three deposits currently defined relate to mafic metavolcanic rocks. Visible gold occurs in many prospects and is usually associated with sulfides including pyrite, chalcopyrite, arsenopyrite, galena, and, less often, sphalerite and pyrrhotite. Other metals reported are cobalt, copper, silver and molybdenum (Gebert, 1993). Timing of mineralization remains unclear. Most gold occurrences are reported to be hosted by D<sub>2</sub> structures including isoclinal folds and shear zones at greenschist facies. Shear zones of varied orientations and a few meters to hundreds of meters wide are the most common host to gold-bearing quartz-carbonate veins (Gebert, 1993). Several VMS showings are also reported near felsic centers throughout the HBB. One of these occurs in the Flake Lake region immediately SW of the study area. Given the numerous HBB mineral commodities it is key to establish whether any of these settings may extend in the EL which has been generally overlooked by most mapping parties in the past principally because of its slightly higher grade of metamorphism.

## **DESCRIPTION OF EL ROCK UNITS**

### ***Stratigraphy***

The scale of mapping was too coarse to breakdown obvious lithological variations within most supracrustal rock sequences. Although iron formation, metapsammite, and felsic metavolcanic rock interbeds define good markers in this rock sequence, no exact facies relation and internal stratigraphy could be clearly established. Intensive ductile deformation and metamorphic recrystallization due to the proximity of the EL marginal shear zone, termed the OPIK Shear Zone (OSZ), (Fig. 2) has obscured most primary stratigraphic relationships and structures that are critical for a rigorous stratigraphic description and interpretation of the rock sequence. Six principal rock types have been identified in the area of investigation. Though their age relationships are not yet determined by precise age dating methods, they are presented herein in a younging order identified from field relationships. Thus, combining the structural and cross-cutting relationships with the nature of xenoliths, the suggested sequence of rock emplacement is; 1) metavolcanic rocks, 2) migmatite-gneiss protoliths, 3) metagabbros, 4) porphyritic metagranite, 5) equigranular metagranite, and 6) dolerites and other anorthositic and felsic dikes (Fig. 3). The basement to the mafic metavolcanic rock sequence has not been found. Zircon inheritance may be expected and could hint at basement in the region.

### ***Supracrustals***

Interpreted as the oldest rock sequence in the region, mafic metavolcanic rocks commonly exhibiting flattened pillows (15 to 50 cm long; 2 to 10 cm thick) with <5 cm thick selvages form the dominant supracrustal rock unit in the EL. In places, mafic metavolcanics display schistose to ‘striped’ textures generally defined by epidote-rich bodies (pillow cores, selvages, interpillow fills, and veins) as well as uneven embedded small size (<15 cm across) pillows. Locally, 1 to 300 m thick felsic metavolcanic rocks are interleaved with the mafic rocks. Rare iron formation and metapsammite interbeds less than 4 m thick are also present, but are too thin to report on the map. As such, the supracrustal rock sequence of the EL may be considered analogous to the Yellowknife-type volcanic belts defined by Padgham (1985) in the southern Slave Craton. Where best preserved and exposed, mafic metavolcanic rocks define a 1000 to 2000 m wide, NE-trending zone between the Four Lakes area and the OSZ (Fig. 2). Westward of the Four Lakes area toward the HBB, mafic metavolcanic rocks define 20 to 500 m thick strips and spindle-shaped lenses between metagabbro and metagranite intrusions (Fig. 2). Lenses of similar sizes seem to occur southward of Spyder River and northward of the Angimajuk River (Fig. 2). Northeast of the Four Lakes area, where migmatization picks up, the many mafic rafts (typically individual or aggregates of 5 cm wide x 20 cm long) occurring in the metagranitoids are related to mafic metavolcanic protoliths and define a NE-trending corridor approximately 1km wide (Fig. 2).

### ***Migmatitic domain***

Partially molten granitic gneiss and abundant deformed inclusions of mafic gneiss, centimeters to few meters across, represent protoliths of early-emplaced felsic magmatic bodies within and across the supracrustal rock sequence (Figs. 1+2). This unit forms a 300 to 1000 m wide, pinching and swelling, NE-trending strap zone along the eastern edge of the mapped area and seems to extend eastward toward a migmatite-gneiss domain that extends considerably east of the EB and beyond the mapping area. The amount of melt within this domain is variable, but generally less than 20 vol.% of the rock. Uneven leucosome veinlet swarms of 300 to 1000 m wide occur in all rock units. Most leucosomes observed tend to pond parallel or cross-cut nearly perpendicular to a preexistent fabric in hosting supracrustal material. They are inferred to illustrate westward melt flow from deeper to shallower crustal levels. The related melanosome are rarely observed. The classification and petrogenesis of the migmatites will not be presented in this work and should be subject of further mapping.

### ***Metagabbro***

Biotite-bearing metagabbro define a group of mafic intrusions that were mapped in a small area north of Spyder River, between the Four Lakes area and the OSZ. These intrusions cut equigranular metagranite and supracrustal rocks in the form of 300 to 2000 m wide sheet-like magmatic bodies seemingly extending westwards where they may connect with the Flake Lake gabbroic batholith in the neighbouring HBB (Fig. 2). Sheet-like bodies of similar size also occur locally within the equigranular metagranite.

### ***Porphyritic metagranite***

The porphyritic metagranite extends from the south central part to the northern end of the mapped area. It nearly stitches the contact between migmatitic gneisses to the east and the Angimajuq Metagranitoid Complex (AMC) to the west (Fig. 2). This unit pinches and swells between 1 to 3 km wide along-strike defining a sheet-like magmatic body extending northwards parallel to the EB. Its porphyritic texture illustrates a two-stage cooling history subsequent to initial emplacement of the magmatic body at deeper crustal levels before it reached shallower crustal levels.

### ***Equigranular metagranite***

The phaneritic equigranular metagranite represents another group of intrusive felsic magmatic bodies underlying most of the southern end of the mapped area and likely connecting to the AMC in the northwest (Fig. 2). This intrusive rock type occurs along a 0.5 to >3 km wide strap zone pinching in the Four Lakes area and swelling southwestward toward Spyder Lake in the HBB. Westward, it forms small magmatic bodies (200 to 2000 m across) of varied shapes within the metagabbro (Fig. 2). Variably striking granitic and pegmatitic dikes of less than a meter thick and few tens of meters long occur principally within the metagranites but some dikes are also clearly cutting mafic magmatic rocks.

### ***Dolerite dikes***

NE-trending dolerite dikes cut EL magmatic rocks. Dikes are <1 to 20 m wide, and kilometers long. Anorthosite dikes of similar orientation and less than 10 m thick were observed in two locations within the metagabbro outcropping between the Four Lakes area and the OSZ (Fig. 2).



### ***Magnetic Susceptibility***

Most rock units of EL exhibit contrasting magnetic susceptibility (Table 1) a useful physical property for detailed mapping in the region..

### ***Contact relationships***

Iron formation in supracrustals is generally gossanous and shows a rusty conformable sharp contact with the surrounding mafic metavolcanic rock. Metapsammite and felsic metavolcanic rock interbeds have sharp contacts with no noticeable mineral transformation in the embedding rock sequence. In general, supracrustal rocks of the EL are tectonically bounded in the north against the AMC by the OSZ which defines a >1 km wide reverse shear zone (Figs. 2+3). West of the Four Lakes area, supracrustals appear to be locally conformable to the intruding magmatic bodies. Elsewhere, mafic rafts, well defined in the metagranites, are usually conformable to their host rocks. The former commonly depict sharp intrusive contacts with no visible reaction seams or grain-size reduction in the latter. Generally, proximal rafts are angular and abundant in the intrusion margins, whereas distal rafts are scarce and show a more rounded shape due to deformation and, possibly, to modifications subsequent to partial assimilation by the host magma.

The contact between the migmatite-orthogneiss and metagranites or between the porphyritic and the isogranular metagranites has not been observed. However, rafts of the mafic veined gneiss in the metagranites depict sharp intrusive contacts defined by a sharp lithological change with no distinctive reaction selvage. The boundary between the isogranular metagranite and the metagabbro along the OSZ west of the Four Lakes area displays similar characteristics (Fig. 4c).

Granitic dike swarms cutting the supracrustals display contacts with no noticeable textural or mineralogical transformation in the immediate host rocks. These dikes seem to have developed within <100 m wide mantling zone around the AMC for which they represent intruded apophyses into the host supracrustal rock sequence. By contrast, the westward decreasing of granitic leucosomes likely depicts an oblique cross section exhibiting deeper crustal levels in the eastern margin of the EB and shallower levels in the HBB to the west.

The lack of contact aureoles and related hornfels textures around any granitic body suggests that the varied intrusive bodies in the mapped area were thermally in equilibrium with their host rocks during their emplacement. Some dolerite dikes lacking contact selvages and grain size reduction in their wall rocks suggest a similar thermal equilibrium as evidenced by granitic bodies, whereas others showing chilled margins of few centimeters thick indicate a difference in temperature between the dike intrusions and their hosts. Thus, the first type of dolerites can be attributed to Archean intrusions, whereas the second can be considered as Proterozoic in age.

### ***Lithology and metamorphic evolution***

Irrespective of the rock type described above, the grain size varies from fine ( $\leq 100 \mu\text{m}$ ) to coarse ( $\geq 300 \mu\text{m}$ ) and corresponds to varied textures ranging from mylonitic to porphyro-phaneritic (Fig. 5). The mineralogical composition of the rock units is summarized in Tables 2+3. Petrographically, neither the porphyritic nor the isogranular metagranitoids is mineralogically homogeneous. They can both be divided into biotite bearing metagranites and amphibole $\pm$ biotite bearing metagranites. Apart from the dolerites and the anorthosites in which two parageneses are distinguished, all the rock units variably show three generations of mineral assemblages ( $M_0$ - $M_3$ ). X-ray diffraction indicates that amphibole has the composition of magnesio-hornblende in mafic metavolcanic rocks, magnesio-hornblende or ferro-tschermakite composition in the metagabbro, metagranite and the migmatitic-gneiss, and tirodite (alkali amphibole) in iron formation and dolerites and metapsammites, and tremolite in dolerites. Plagioclase is generally albitic, but locally displays optical zoning in felsic intrusions. The assemblages  $M_0$ - $M_3$  can be distinguished in pre-metamorphic, prograde, peak metamorphic, and retrograde mineral assemblages.

### ***Pre-metamorphic mineral assemblages***

Pre-metamorphic mineral assemblages in the supracrustal rocks and the migmatites are texturally very difficult to distinguish, because of intensive hydrothermal retrogression and dynamic recrystallization. On the contrary, texturally preserved magmatic mineral assemblages ( $M_0$ ) including amphibole, orthoclase, and zoned plagioclase are common in the granitoids and dolerites + anorthosites (Table 2). Pyroxene has not been preserved. These  $M_0$  minerals are illustrations that the intrusive rocks post-date emplacement of their hosts. They are generally relics of large crystals defining porphyroclastic and porphyritic textures in granitoid intrusions and dolerites + anorthosites, respectively (Fig. 5).

### ***Prograde mineral assemblages***

Supracrustal rocks and migmatitic gneiss generally show overprinting of two dynamically recrystallized mineral assemblages  $M_1$  and  $M_2$  defining varied porphyroclastic to mylonitic textures (Table 2). By contrast, only one dynamically formed metamorphic assemblage ( $M_2$ ) is found in the intrusive rocks. It is usually in the form of fine-grained layers wrapped around relics of magmatic phenocrysts. Amphibole + biotite + chlorite pertaining to  $M_1$  assemblages generally depict polygonal arcs due to a crenulated  $S_n$  foliation. The crystallographic preferred orientation (CPO) exhibited by  $M_2$  minerals illustrates  $S_{n+1}$  fabric axial planar to these microfolds of  $S_n$  foliation (Fig. 5).  $M_1$

characterizes epidote-amphibolite facies, whereas the occurrence of muscovite + calcite in  $M_2$  assemblages suggests upper greenschist metamorphic grade. All these medium- to low-grade mineral associations suggest intensive deformation assisted hydrothermal retrogression of the volcanic and intruded igneous protoliths from magmatic to greenschist facies metamorphic conditions. However, the occurrence of isotropic garnet due to the breakdown of chlorite (Bucher and Frey, 1994) in the felsic metavolcanic rocks, in particular, demonstrates that the corresponding hydrothermal mineral assemblages suffered dehydration mineral reactions characterizing prograde metamorphism during formation, at least, of  $M_1$  mineral assemblages and  $S_n$  fabric. This prograde metamorphism occurred with partial melting of early-emplaced granitic rocks outcropping in the eastern margin of the EB (Fig. 13c).

### ***Peak mineral assemblages***

The peak mineral assemblages include amphibole + biotite + plagioclase in the mafic metavolcanic rocks and the metagabbro, garnet + biotite in the felsic metavolcanic rocks, and amphibole + biotite + plagioclase + orthoclase in the migmatitic gneiss and the metagranites. In the magnetite-bearing metabasalts, in particular, the related peak P-T conditions as inferred from coexisting epidote and chlorite have the minimum values of ca. 3.3 kb and ca. 560 °C (Apted and Liou, 1983). This indicates that hydrothermal alteration of the magmatic protoliths was not continuous. Furthermore, the presence of peak metamorphic minerals in both  $M_1+M_2$  assemblages in the supracrustal rocks and the migmatitic gneiss shows that prograde metamorphism culminated during the early stages of  $S_{n+1}$  fabric development. It follows that the metagranite and metagabbro were emplaced, at least partly, during the peak metamorphism occurring synchronously with partial melting of early-emplaced felsic intrusions. The spatial distribution of the corresponding leucosomes on the east side of the studied area relates to the deepest crustal level (migmatite orthogneiss) whereas the shallowest crustal levels are preserved in the HBB rocks where hydrothermal carbonate-chlorite alteration prevailed. The nature of the boundary between crustal levels remains unclear but it is proposed that this is either gradual or tectonically telescoped. Evidence of telescoping does not seem obvious thus the gradual transition of crustal levels is currently the preferred option. Mapping metamorphic conditions of the different crustal levels is further challenged by pervasive retrogression overprinting prograde metamorphic assemblages.

### ***Retromorphic mineral assemblages***

The switch from prograde to retrograde metamorphism during development of  $M_2$  mineral assemblages is well indicated by the appearance of muscovite in the felsic metavolcanic rocks, chlorite

+ calcite in the metagabbros, and muscovite + chlorite in the metagranites (Table 3). The corresponding metamorphic conditions are those of the upper greenschist facies under which  $S_{n+1}$  fabric continued to develop. Thus, the  $S_{n+1}$  foliation can be regarded as a diaphrotitic fabric. Late greenschist static recrystallization resulted in development of the  $M_3$  retromorphic assemblages in all the rock types (Table 2). The occurrence of these  $M_3$  minerals lacking any CPO shows that the greenschist retromorphism outlasted deformation. The presence of  $M_3$  minerals in the Proterozoic dolerites, in particular, illustrates a post-Archean thermal event likely due to the Thelon Orogeny. However, this interpretation does not preclude the presence of Archean  $M_3$  mineral phases; they are simply hard to distinguish texturally.

The metamorphic evolution during which the  $M_0$ - $M_3$  mineral assemblages described above developed was interpreted by Thompson (1997) as a complex interference of successive thermal events due to emplacement of three generations of Archean granitoids. However, apart from garnet-bearing metarhyolites that may reflect local intrusion-related thermal metamorphism, signatures of Archean granitoids as key thermal engines in the metamorphic history of the EL is not obvious based on our field and petrographic observations. For instance, no characteristic hornfels texture with diagnostic contact aureole minerals such as olivine, pyroxene, cordierite, and andalusite, and staurolite that should be present if the EL suffered contact metamorphism have not been documented. Also, most mineral phases are recurrent in all the rock units (Tables 2+3) so that it would be very challenging to map out the metamorphic zones around the Archean magmatic intrusions. Thus, it follows that the ELu metamorphic history in general is best interpreted in terms of post-hydrothermal prograde and retrograde regional metamorphism with limited or no significant thermal input from the intruded magmatic bodies. The belt rock package was later affected by a strain-free Paleoproterozoic thermal event due to the Thelon Orogeny.

## **GEOCHEMISTRY**

### ***Metamafic igneous rocks***

On most classification diagrams, both the mafic metavolcanic rocks and metagabbros plot as a fractionation trend ranging in composition from subalkaline basaltic to andesitic (Fig. 6), but which on the  $Zr/(P_2O_5) - TiO_2$  plot correspond principally to tholeiitic flows. The alkali basaltic signatures of the rocks are likely due to fractionation. They yield  $50.99 \pm 3.27$  wt.%  $SiO_2$ ,  $14.18 \pm 1.93$  wt.%  $Al_2O_3$ ,  $13.98 \pm 2.89$  wt.%  $Fe_2O_3T$ , and  $9.09 \pm 2.78$  wt.%  $CaO$  average and standard deviation values recalculated on a volatile-free basis. There is no clear regular variation of major elements with any common fractionation index, although a rough increase in  $TiO_2$ ,  $P_2O_5$ , La and Sm with increasing Zr

may be observed. However, these chemical analyses allow distinction of; 1) low-titania ( $< 1.00$  wt.%  $\text{TiO}_2$ ) and medium- to low-alumina ( $\leq 17.00$  wt.%  $\text{Al}_2\text{O}_3$ ) and 2) high-titania ( $1.00$  wt.%  $< \text{TiO}_2 < 3.00$  wt.%) and medium- to high-alumina ( $12.00$  wt.%  $< \text{Al}_2\text{O}_3 < 19.00$  wt.%) magmatic suites. Titanium-depleted rocks show Yb contents ( $2.60 \pm 1.28$  ppm;  $n = 16$ ) comparable with Mg-tholeiites, whereas variable Yb values ( $2.66 \pm 1.25$  ppm;  $n = 37$ ) characterizing both Mg- and Fe-tholeiites (Hall and Plant, 1992) are indicated by Ti-enriched suite. On  $\text{TiO}_2$ - $\text{Al}_2\text{O}_3$  plot (Fig. 6), Ti-enriched suite displays a fan-shaped distribution, which, according to Gaboury (2006), is characteristic of subvolcanic intrusions with good mineralization prospectivity as compared to the Ti-depleted intrusive rocks with a restricted  $\text{TiO}_2$  variation defining late- to post-volcanic. All these features agree with  $51.1 \pm 3.42$  wt.%  $\text{SiO}_2$ ,  $1.40 \pm 0.46$  wt.%  $\text{TiO}_2$ ,  $14.90 \pm 1.65$  wt.%  $\text{Al}_2\text{O}_3$ , and  $93 \pm 55$  ppm Zr contents indicated by the mean composition ( $n = 36$ ) of the Flake Lake mafic metavolcanic rocks in the HBB and located immediately west of the mapping area. Indeed, a  $\text{TiO}_2$ - $\text{Al}_2\text{O}_3$  plot of mafic metavolcanic rock samples from the EL and the Flake Lake suite in the HBB indicates three rock types (A-C) with only one EL rock sample in the A field probably reflecting sampling deficiency and/or the scarcity of A type rocks (Fig. 6). Compared with other greenstone belts, the gold-rich gabbros from the Kalgoorlie greenstone belt (Bateman et al., 2001) show the same pattern, whereas rocks from the Yellowknife and Red Lake greenstone belts straddle the boundary between B and C fields (Fig. 6). The EL metagabbros show the same bimodal distribution between B + C groups. These relationships suggest that the HBB is continuous to the EB which suggests that the latter may also have good gold potential if gold relates to such compositions.

Varied Mg# [ $\text{Mg}/(\text{Mg}+\text{Fe}^{2+})$ ] calculated on the basis of  $\text{Fe}^{3+}/\text{Fe}^{2+} = 0.2$  in both the HBB+EL rocks ( $15.20 \pm 5.80$  and  $15.81 \pm 6.02$ , respectively) denote important fractionation of their protolith magmas. Indeed, very low ( $\leq 0.7$ ) to high ( $> 1.0$ ) La/Nb ratios exhibited by these rocks suggest that they originated from both enriched and depleted mantle sources (Sun and McDonough, 1989). On chondrite-normalized REE plot, both Ti-depleted and Ti-enriched rocks break down into flat REE- and LREE-enriched sub-suites comparable to Island-Arc Tholeiites (IAT) and related high-K calc-alkaline basalts, respectively (Fig. 7). The flat REE pattern is also indicated by MHBR; and both flat REE and LREE-enriched suites depict a weak Eu negative anomaly suggestive of limited plagioclase fractionation under oxidizing conditions during crystallization of the parental magmas (Hess, 1989). Conversely, N-MORB-normalized profiles regardless of the rock group depict highly incompatible element enrichment including Th + Ce, and significant Nb (Ta) and Ti depletion characteristic of magmas generated in active subduction margin settings (Fig. 7). The mean composition of the reference greenstone belts principally compare with the flat REE suite (Fig. 7).

On Ti/V ratios and Ti-Zr-Y ternary diagram most samples plot in the Mid-Ocean Ridge Basalt (MORB) and Volcanic-Arc Basalt (VAB) fields with a few plotting as Within-Plate Basalts (WPB) (Fig. 8). The Th-Hf-Ta ternary plot confirms this distinction of magmas (Fig. 8). The reference greenstone belts yield similar chemical affinities (Fig. 8).

### ***Metamorphosed felsic igneous rocks***

The felsic metavolcanic rocks range in composition from dacitic to rhyolitic lavas (Fig. 9), whereas the felsic intrusive rocks straddle the boundary between granodiorite and granite fields (not shown). Both felsic rock types yield an average composition of  $70.89 \pm 3.99$  wt.% SiO<sub>2</sub>,  $2.49 \pm 1.14$  wt. % CaO,  $0.33 \pm 0.20$  wt. % TiO<sub>2</sub>,  $13.74 \pm 2.50$  wt. % Al<sub>2</sub>O<sub>3</sub>, and  $5.17 \pm 3.89$  wt.% Fe<sub>2</sub>O<sub>3</sub>T. Generally, CaO, Fe<sub>2</sub>O<sub>3</sub>, MgO, and TiO<sub>2</sub> decrease with increasing SiO<sub>2</sub> indicating magmatic differentiation of the rock protoliths. Although Fe<sub>2</sub>O<sub>3</sub>T and TiO<sub>2</sub> correlate positively with MgO along two magmatic trends, felsic magmatic suites are difficult to distinguish, possibly, because the metafelsic igneous rocks represent the most fractionated magmas in the area. Indeed, considering  $Fe^{3+}/Fe^{2+} = 0.2$ , the rocks yield mean Mg# value [ $Mg/(Mg+Fe^{2+})$ ] of  $10.20 \pm 5.66$  with lower values ( $< 10.00$ ) generally corresponding to intruded felsic bodies. Furthermore, positive correlation between Ce and La, or Hf and Zr suggests that the metafelsic igneous rocks could be comagmatic (Fig. 9b). On K<sub>2</sub>O vs. SiO<sub>2</sub> and AFM diagrams (not shown), they span a composition ranging from tholeiitic to high-K calc-alkaline series. The corresponding agpaitic index (molar (Na<sub>2</sub>O+K<sub>2</sub>O)/Al<sub>2</sub>O<sub>3</sub>) is  $0.6 \pm 0.12$ , which together with the aluminum saturation index (molar A/CNK) of  $1.10 \pm 0.20$  demonstrate that they derived from peraluminous to slightly metaluminous I-type melts (Chappell and White, 1992). All these geochemical characteristics are similar with those of the Flake Lake felsic suite in the HBB.

On chondrite-normalized profiles, the felsic metavolcanic rocks show a relatively flat REE pattern with a weak Eu negative anomaly, whereas the metafelsic intrusive rocks characterize by LREE enrichment and a slight Eu positive anomaly (Fig. 9c). Like for the mafic metaigneous rocks, Eu anomalies in these rocks possibly reflect limited plagioclase fractionation in oxidizing conditions (Hess, 1989). However, both rock groups on ORG-normalized plot exhibit a pronounced Nb (Ta) negative anomaly associated with LILE (K, Rb, Ba, and Th) enrichment and HSFE (Ce, Hf, Zr, Sm, Y, Yb) depletion similar to Volcanic Arc Granites (VAG) (Pearce et al., 1984). Indeed, most of these rocks plot as orogeny related A-type VAG on various tectonic setting discrimination diagrams (Fig. 10). Few samples characterizing as anorogenic A-type Within Plate Granites (WPG) are likely due to fractionation (Fig. 10). Samples of the Flake Lake suite depict similar contrasting geochemical features, which, again, suggest that HBB and EB are continuous.

### ***Dolerites***

Like the metagabbros and the mafic metavolcanic rocks, the dolerites depict tholeiitic basalts to basaltic andesites affinities. They yield  $49.72 \pm 0.55$  wt.%  $\text{SiO}_2$ ,  $13.31 \pm 0.59$  wt.%  $\text{Al}_2\text{O}_3$ ,  $16.62 \pm 1.17$  wt.%  $\text{Fe}_2\text{O}_3\text{T}$ , and  $9.36 \pm 0.67$  wt.%  $\text{CaO}$  average and standard deviation values recalculated on a volatile-free basis. As compared to their mafic meta-igneous hosts, the dolerites are particularly highly Ti-enriched (generally  $> 2.00$  wt.%  $\text{TiO}_2$ ) and moderately Al-depleted ( $< 14.00$  wt.%  $\text{Al}_2\text{O}_3$ ). These rocks plot mostly in the B field of the three HBB magmatic suites defined to date. They correspond to the Ti+LREE enriched sub-suite of the EL mafic rocks compared to which they appear to be less fractionated. The related Ti/Y and La/Nb ratios ( $349.3 \pm 11.7$  and  $1.8 \pm 0.1$ , respectively) show that the dolerites originated from a deep mantle source.

## **STRUCTURAL GEOLOGY**

In the following, structures related to a deformation phase  $D_n$  are named  $S_n$  (foliations),  $L_n$  (lineations),  $F_n$  (folds), etc. However, different deformation phases do not necessarily designate temporally separated events. Instead, they represent steps of progressive deformation that can be recognized and separated in terms of their fabrics, timing by overprinting relationships, kinematics, and sometimes metamorphic grade as well.

### ***Fabric elements and deformation phases***

Bedding  $S_0$  is defined by the intercalation of various supracrustal rock types. In mafic metavolcanic rocks, flattened pillows together with zoisite-rich veins and preferred aligned amphiboles outline a pervasive bedding parallel fabric  $S_0/S_1$  (Fig. 11). This composite surface corresponds to the  $S_n$  fabric illustrated by  $M_1$  mineral assemblages. It is defined by oriented biotites in felsic metavolcanic rocks, aligned amphibole and magnetite in metapsammitic rocks, and a gneissic alternation of magnetite  $\pm$  biotite-rich and quartzofeldspathic layers in iron formation. It is defined by alternating amphibole + biotite-rich and quartzofeldspathic layers in mafic gneiss, and oriented biotites and quartzofeldspathic layers in felsic gneiss (Fig. 11). Both  $S_0/S_1 + S_1$  are transposed by  $F_2$  folds into a discrete  $S_1/S_2$  axial planar foliation corresponding to the  $S_{n+1}$  fabric defined by  $M_2$  mineral assemblages and that is commonly defined by the assemblage chlorite  $\pm$  muscovite. By contrast, amphibole  $\pm$  biotite metagabbros and biotite  $\pm$  amphibole metagranites exhibit an unfolded penetrative foliation axial planar to folds of leucosomes and which is thus distinguished as an  $S_2$  fabric. This surface is defined by the CPO of the  $M_2$  mineral assemblages chlorite + amphibole  $\pm$  biotite  $\pm$  magnetite in metagabbros

and biotite + chlorite  $\pm$  amphibole  $\pm$  titanite in metagranites. It shows that  $D_2$  is the last fabric-forming deformation in the area.  $S_1/S_2$  and  $S_2$  foliations are sub-parallel and dip steeply west- to northwards (Figs. 2+11). West of the studied area, their traces deflect progressively either northwards or southwards to define a foliation triple junction with the N-S trending HBB.

A faint  $L_2$  stretching lineation on both  $S_1/S_2$  and  $S_2$  surfaces is common. Regardless of the rock unit,  $L_2$  is generally illustrated by stretched quartz and elongated quartzofeldspathic aggregates. It has a radial distribution and plunges steeply northwards (Fig. 11).

### ***Folds***

$F_1$  folds of bedding  $S_0$  have not been observed, possibly, due to strong post- $D_1$  overprint and a lack of time to document these challenging features. On the other hand, tight to open parasitic  $F_2$  folds of  $S_0/S_1$  and  $S_1$  foliations in the metavolcanic rocks and the migmatitic gneiss, respectively, are common.  $F_2$  folds of leucosomes and quartz veins in all rock units are also found. The enveloping surface of these  $F_2$  structures delineates short wavelength folds pertaining to large-scale  $F_2$  synclines and anticlines cored by supracrustal rocks and magmatic bodies, respectively (Fig. 2). The related fold hinges have a radial distribution and are coaxial with  $L_2$  stretching lineations. This, together with the parallelism between  $S_0/S_1$  and  $S_2$  foliations shows that the large-scale  $F_2$  are curvilinear isoclinal folds (Fig. 12).

On stereograms,  $S_1/S_2$  and  $S_2$  align along prominent great circles, which, together with their map traces, suggest the presence of  $F_3$  folds in the area. Also, it is important to notice the presence of outcrop-scale cryptic folds of supracrustals generally found along the EL E-W segment in the contact zones between the magmatic bodies and their hosting metavolcanic rocks. These structures are buckled, inconsistently verging, parasitic intrafolial folds including box folds generally nucleated around pillow lavas. They are steeply northwards plunging décollement folds with axial plane traces oblique ( $30-90^\circ$ ) to  $S_2$  foliation in the metagabbros (Figs. 11c+d). This shows that they are  $D_3$  structures illustrating rheological contrast between interleaved metagabbros and mafic-pillowed flows. Local  $F_3$  crenulation folds of  $S_2$  fabrics in the intruded metagranitoids represent additional  $D_3$  structures occurring in the EL E-W segment.

### ***Kinematics***

The main kinematic indicators observed in the area are shear zones, boudins and folded veins related to the last  $D_2$  event.



A variety of discrete shear zones have been mapped. Most define conjugate strike-slip geometries but reverse shear zones are also clearly defined in  $\geq 1000$  metres wide curved corridor bounding the EL to the north against the AMC between the HBB and the EB. This corridor of high strain is referred to as the Opik Shear. Rare thrust zones principally formed within the metagabbro at the NW corner of the mapped area are also documented. When combined, the trends and kinematics of these discrete shear zones do not indicate a consistent sense of shear, which indicates a  $D_2$  dominant coaxial strain (Mvondo et al., 2010). They are preferred alteration zones usually filled with quartz veins, sulfides, carbonates, and/or epidote-rich leucosomes (Fig. 13). A more detailed description of these structures can be found in Mvondo et al. (2010).

Boudinage structures including foliation boudins, stretched and boudinaged quartz veins and leucosomes, and stretched and pulled apart mafic septa are common. These structures occur on sub-horizontal and sub-vertical outcrops comparable to (Y, Z) and (X, Z) planes of the finite strain ellipsoid, respectively. They are mostly symmetric on (Y, Z), whereas asymmetric and symmetric boudins (~10 % and ~90 %, respectively) appear on (X, Z) outcrops.

Variably folded leucosome and quartz veins as well as dolerites and granitic dikes are found locally. The corresponding folds show inconsistent vergence and suggest a major  $D_2$  flattening with sub-horizontal foliation parallel stretching (Fig. 13).

All together, the main kinematic indicators consistently show that  $D_2$  strain is dominantly a vertical general flattening strain that occurred with E-W maximum compression and N-S minimum extension. Asymmetrical boudins on (X, Z) planes, together with reverse shear zones, illustrate a simple shear component consistent with a transpressive bulk strain.

## **CONTROLS ON MINERALIZATION**

### ***Alteration patterns***

Despite no specific zone of intense alteration was observed therein, the mapped area could be divided into two domains of distinctive alteration styles (Fig. 14). Chloritization, sericitization, and epidotization are common to all the rock units, but some rock types appeared variably silicified and hematized. Silicification is defined by <10 centimeters wide and a few meters long quartz veins containing chlorite  $\pm$  sulfides  $\pm$  muscovite along  $D_2$  shear zones and fractures. Local granitic leucosomes and/or epidote-rich veins sandwiched between hematite infillings in the metagranites show the same habits but could be altogether of a younger age. Carbonate + chlorite alteration like in the neighbouring HBB occurs principally west of the Four Lakes area (Fig.14). It is illustrated by millimeters thick and several meters long, discontinuous calcite and sulfide veins formed along shear planes and shear band boudin necks, tension gashes, and foliation planes in the  $D_2$  related

microlithons. Owing to the competence contrast between the metavolcanic rocks and their intrusive rocks as illustrated by décollement  $F_3$  folds, saddle-type veins may also be found. All these features indicate a dominant structural control of the rock alteration like in the HBB (see Mvondo et al., 2010 for illustrations).

### ***Sulfide assemblages***

No visible gold mineralization has been observed, but its presence can be inferred from sulfides with which it is usually associated (Boyle 1987) and that occur in most EL rock units. Sulfide minerals are generally in trace amounts but are relatively more abundant in the iron formation and the metapsammite, which thus appear as distinctive mineralized layers within the supracrustal rock sequence and the migmatite orthogneiss. Iron Formations forms few meters thick and tens of meters long rusty rock reefs in migmatite orthogneiss (Fig. 2) and are composed of quartz + magnetite + amphibole + chlorite ± zoisite ± sulfides ± apatite. Rare metapsammites occur as few centimeters wide and less than a meter long light gray, coarse-grained boudins in the metagranitoids and consist of quartz + chlorite + muscovite + plagioclase + magnetite + amphibole ± biotite ± zoisite ± titanite ± sulfides ± hematite. Sulfide minerals generally include pyrite, chalcopyrite, and sphalerite. Arsenopyrite and pyrhotite are scarcely found.

Detailed micro-structural and textural analysis indicates the presence of three generations of sulfides associated with the  $M_1$ - $M_3$  metamorphic mineral assemblages.  $M_1$  sulfides are rare, but their presence is well illustrated in the metapsammite and the migmatite orthogneiss in which they are microfolded and form inclusions in titanite along  $S_1$  fabric (Fig. 15a+b).  $M_2$  sulfides are more common. They occur as elongated blasts with irregular boundaries crystallized along  $S_2$  foliation and  $D_2$  shear zones (Fig. 15a-c). The  $M_3$  generation corresponds to euhedral to subhedral crystals of varied sizes lacking any CPO (Fig. 15). They locally show inclusions of early-formed sulfides (Fig. 15e+f). The three generations of sulfides are suggestive of syn- to post-tectonic remobilization of pre-metamorphic sulfide deposits. However, syn- $D_2$  intrusions with disseminated  $M_2$ + $M_3$  sulfides suggest coeval introduction of juvenile fertile fluids illustrating multiple phases of mineralization. Further field studies combined with isotopic and absolute age data would provide further constraints to this interpretation.

### ***Geochemical anomalies***

Assay results show that, most of the rock units including the metabasalts, the metagabbros, the metapsammite, iron formation, the migmatitic gneiss, and the

metagranites yield Au + As + Cu + Zn values that may be considered above background (Figs. 17-20). These elements generally show no clear inter-element correlation or any regular variation with any common fractionation index. However, a broad Zn increase with increasing TiO<sub>2</sub> contents in felsic meta-igneous rocks and Ti-enriched flat REE metagabbros suggests that the occurrence of this mineralization is magmatically controlled (Fig. 16). Indeed, gold in Ti-enriched flat REE metagabbros tends to be more prominent than in the other main rock units (Figs. 16+17). Arsenic concentrations show a similar trend, whereas greater amounts of copper seem to occur preferentially within the metagranites (Fig. 19). This, together with the sulfide-bearing metamorphic assemblages (Table 2) shows that the mineralizing fluids have both magmatic and metamorphic origins like in the HBB (Stemler et al., 2006).

## DISCUSSION

### *Strain patterns and regimes*

D<sub>1</sub>–D<sub>3</sub> deformation phases have strongly affected the EL rocks including dominant pillowed metabasalts with subordinate intercalations of metarhyolites, iron formation, and metashales. Hydrothermal mineral assemblages of these rocks were overprinted by epidote-amphibolite prograde metamorphism during intrusion of varied syn-D<sub>2</sub> metagabbro and metagranites. The entire rock mass was further affected by greenschist facies retrogression. Geochemically, all the related rock units consistently indicate a back-arc tectonic setting.

D<sub>1</sub> geometrical structures and strain shape are uncertain due to intensive D<sub>2</sub> overprint. However, prograde metamorphism that accompanied this deformation is an indication that D<sub>1</sub> was a horizontal compression. The latter probably occurred during the closure of the back-arc basin in which the EL supracrustal rocks were deposited.

D<sub>2</sub>-related structures consistently point towards large-scale F<sub>2</sub> curvilinear synclines and anticlines cored by supracrustal and intrusive rocks, respectively. These F<sub>2</sub> folds formed on the sides of a large D<sub>2</sub> domal structure evidenced by; (i) radially plotting coaxial L<sub>2</sub> stretching lineation and F<sub>2</sub> fold hinges, (ii) northwards concave arc-shaped steeply dipping S<sub>1</sub>/S<sub>2</sub> + S<sub>2</sub> foliations, and (iii) curved reverse OPIK shear zone bounding the EL to the north. Sporadically found thrust zones reflect expansion of the domal structure. Nevertheless, the main kinematic indicators demonstrate that D<sub>2</sub> bulk strain is a sub-vertical general flattening dominated transpression occurred with maximum E-W compression and minimum N-S extension. D<sub>3</sub> is a brittle-ductile deformation phase depicting the same strain geometry.

D<sub>2</sub>-D<sub>3</sub> sub-vertical general flattening is illustrative of a protracted regional E-W sub-horizontal compression. This is somewhat contradictory with late retrogression illustrated by D<sub>2</sub> fabrics, as compression tectonics in orogenic belts is generally associated with prograde metamorphism. Owing to D<sub>2</sub> structures and strain geometry however, M<sub>2</sub>-M<sub>3</sub> regressive history is interpreted as illustrating syn-compression exhumation of the belt. The occurrence of migmatitic gneiss along the eastern margin of the EB shows that this exhumation was regionally asymmetric with the EL supracrustal rocks representing the deep level equivalent of the HBB rock sequence (Fig. 3). Causes of the exhumation are yet to be defined.

### ***Geochronology***

The litho-geochemical and structural relationships between the two belts as described above suggest that the EB supracrustal rocks also fall in the age limits of ca. 2716-2663 Ma determined in the HBB and most likely comprise the oldest components of this time sequence (Hebel, 1999). This age range overlaps in part with the ca. 2672-2608 Ma ages (Bevier and Gebert, 1991) yielded by the metagranitoids bounding the HBB suggesting that some intrusions could be syn-volcanic. The margin of the AMC forming the core of a D<sub>2</sub> dome structure of the EL has been dated at ca. 2672 Ma (Bevier and Gebert, 1991) that can be considered to represent the lower and the upper age limit of D<sub>1</sub> and D<sub>2</sub> events, respectively. This interpretation suggests that formation of the protoliths to HBB + EB metavolcanic rocks was, at least partly, syn-tectonic and synchronous with the migmatization. Moreover, it suggests that the onset of gold mineralization and D<sub>1</sub> deformation in the two belts has the minimum age of ca. 2716 Ma (Hebel, 1999) indicated by the Flake Lake felsic suite west of the EL. However, generating absolute geochronological data in the EB remains crucial to confirm these critical timing relationships. Likewise, constraining the timing of D<sub>3</sub> deformation and the diking history requires extended detailed dating (e.g., <sup>40</sup>Ar-<sup>39</sup>Ar dating) and correlations.

### ***Genetic model of the mineralization***

The present study shows that, although occurring in all rock units, Au mineralization and As-Cu-Zn bearing sulfide occurrences are chiefly lithologically and structurally controlled. Indeed, visible sulfide veins along D<sub>2</sub> structures occur mainly within the Ti-enriched flat REE metagabbro suite whose geochemical analysis yields the most significant metal contents (Figs. 16+19). The corresponding mafic metavolcanic rocks also indicate subdued Au contents. Because the studied area suffered prograde and retrograde regional metamorphism, the rock units that were exposed to peak metamorphic conditions and migmatization appear to have valuable mineralization potential. In fact, the presence of textural features characteristic of remobilized pre-metamorphic sulfides in the EL is

evidence that ore deposits therein can be found in rocks of any metamorphic grade including the migmatite orthogneiss.

The relative abundance of gold in syn-D<sub>2</sub> metagabbros suggests that their emplacement occurred with amplification of pre- to syn- D<sub>1</sub> mineralization. In fact, these metagabbros correspond geochemically to subvolcanic intrusions (Fig. 6), which in greenstone belts, are considered as thermal engines and metal suppliers in hydrothermal systems (Galley, 2003, and reference therein; Gaboury et al., 2006). Fluids accumulation and migration continued during and after the D<sub>3</sub> brittle-ductile deformation. However, syn-peak metamorphic mineralization associated with emplacement of the metagabbros and related mafic metavolcanic rocks in the EL raises the question of compatibility with syn-D<sub>1</sub> migmatization, as any mineralizing fluid would have been used to enhance partial melting of the crust (Phillips and Powell, 2009; Tomkins and Grundy, 2009). As such, the incompatibility between migmatization and mineralization suggests that the two phenomenon take place at the same crustal level. Shallow-level migmatization occurring coevally with ascent of mineralizing fluids from a deep-seated magmatic chamber would also lead to a similar type of incompatibility. However, mineralizing fluids derived from a shallow-crustal magmatic chamber pre-dating migmatization at the base of the crust would lead to ore deposits coeval, at list in part, with anatectic melt. Further field studies addressing the mineralization content of the metagabbros and related intrusions and the crustal level origin of the migmatitic orthogneiss, as well as sulfide age data and stable isotope analysis in the belt need to be performed in order to propose a suitable genetic model of the mineralization therein.

## CONCLUSIONS

The EL is dominantly composed of tholeiitic pillowed metabasalts interleaved with subordinate metarhyolites, metadacites, iron formation, and metapsammite. A migmatite orthogneiss in the EL eastern margin represents earlier emplaced magmatic bodies, which together with their hosts were further intruded by varied metagabbros and metagranites. All magmatic components of this Archean rock package derived from mixed upper and lower mantle sources and indicate a back-arc tectonic setting. The entire rock mass was later cut by deep mantle derived NE-trending Paleoproterozoic dolerites. Although the related strain patterns and regime are uncertain, D<sub>1</sub> deformation affecting the migmatite orthogneiss and related supracrustal hosts was probably a horizontal compression accompanied by prograde metamorphism whose peak conditions in epidote-amphibolite facies evolved to greenschist retrogression during D<sub>2</sub> deformation. The latter caused formation of curvilinear large-scale synclines and anticlines mantling a major domal structure centered about the AMC. This deformation is a vertical general flattening dominated transpression that occurred with E-W maximum

compression and N-S minimum extension. D<sub>2</sub> structures were overprinted by D<sub>3</sub> deformation characterizing a long lasting E-W compression and progressive exhumation of the belt. The latter pervasively recorded a strain-free greenschist mineral assemblage illustrating a Paleoproterozoic thermal event. Au-As-Cu-Zn mineralization occurred during or slightly prior to D<sub>1</sub> deformation was remobilized and, possibly, amplified during subsequent tectonometamorphic events and intrusion of Ti-enriched metagabbros.

## **REFERENCES**

### **Apted, J.M. and Liou, J.G.**

1983: Phase relationships among greenschist, epidote-amphibolite, and amphibolite in a basaltic system; *American Journal of Science*, v. 283, p. 328-354.

### **Bevier, M.L. and Gebert, J.S.**

1991: U-Pb geochronology of Hope Bay – Elu Inlet area, Bathurst Block, northeastern Slave Structural Province, Northwest Territories; *Canadian Journal of Earth Sciences*, v. 28, p. 1925-1930.

### **Boyle, R.W.,**

1987: *Gold history and genesis of deposits*: New York, Van Nostrand Reinhold Co, 676 p.

### **Bucher, K. and Frey, M.**

1994: *Petrogenesis of metamorphic rocks*: Berlin, Springer, 318 p.

### **Carpenter, R. L., Sherlock, R. L., Quang, C., Kleespies, P., and McLeod, R.**

2003: Geology of the Doris North gold deposits, northern Hope Bay volcanic belt, Slave structural province, Nunavut; *Geological Survey of Canada, Current Research 2003-C6*, 10 p.

### **Chappell, B. W. and White, A. J. R.**

1992: I- and S-type granites in the Lachlan Fold Belt; *Transactions of the Royal Society of Edinburgh, Earth Sciences*, v. 83, p. 1–26.

### **Gaboury, D.**

2006: Geochemical approaches in the discrimination of synvolcanic intrusions as a guide for volcanogenic base metal exploration: an example from the Abitibi belt, Canada; *Applied Earth Science (Trans. Inst. Min. Metall. B)* v.115, p. 71-79.

### **Galley, A.G.**

2003: Composite synvolcanic intrusions associated with Precambrian VMS-related hydrothermal systems; *Mineralium Deposita*, v. 38, p. 443-473.

**Gebert, J.S.**

1990: Geology of the Hope Bay and Elu Inlet metavolcanic belts, Bathurst Block, northeastern Slave province, N.W.T.; Abstracts in Exploration Overview 1990; Northwest Territories, p. 26.

1993: Geology and Mineral potential of the Archean Hope Bay and Elu Inlet volcanic belts, northeastern Slave structural province, District of Mackenzie, N.W.T.; Northern Affairs Program, Northwest Territories Geology Division, EGS Paper 1993-1, 103 p.

**Goodwin, A.M., Lambert, M.B., and Ujike, O.**

2006: Geochemical and metallogenic relations in volcanic rocks of the southern Slave Province: implications for late Neoproterozoic tectonics; Canadian Journal of Earth Sciences, v. 43, p. 1835-1857.

**Hall, G.E.M and Plant, J.A.**

1992: Application of geochemical discrimination diagrams for the tectonic interpretation of igneous rocks hosting gold mineralization in the Canadian Shield; Chemical Geology, v. 95, p. 157-165.

**Hebel, M.U.**

1999: U-Pb geochronology and litho-geochemistry of the Hope Bay greenstone belt, Slave Structural Province, Northwest Territories, Canada; MSc. thesis, University of British Columbia, Vancouver, British Columbia, 96 p.

**Hess, P.C.**

1989: Origins of igneous rocks; Harvard University press, Cambridge, Massachusetts, London, 336 p.

**Longerich, H.P.**

1995: Analysis of pressed pellets of geological samples using wavelength-dispersive X-ray fluorescence spectrometry; X-Ray Spectrometry, v. 24, p. 123–136.

**Mvondo, H., Lentz, D., and Bardoux, M.**

2010: Tectonometamorphic history and gold mineralization in a link between Hope Bay and Elu greenstone belts, NE Slave Craton; Geological Survey of Canada, Current Research 2010

**Padgham, W.A.**

1985: Observations and speculations on supracrustal successions in the Slave Structural Province; in: Evolution of Archean Supracrustal Sequences, L.D. Ayres, P.D. Thurston, K.D. Card, and W. Weber eds.; Geological Association of Canada, Special Paper 28.

**Pearce, J.A. and Cann, J.R.**

1973: Tectonic setting of basic volcanic rocks determined using trace element analyses; Earth and Planetary Science Letters, v.19, p. 290-300.

**Pearce, J.L., Harris, N.B.W., and Tindle, A.G.**

1984: Trace Element discrimination diagrams for the tectonic interpretation of granitic rocks; *Journal of Petrology*, v. 25, p. 956-983.

**Phillips, G.N. and Powell, R.**

2009: Formation of gold deposits: Review and evaluation of the continuum model. *Earth Science Reviews*, v. 94, 1-21.

**Shannon, A.J.**

2008: Volcanic framework and geochemical evolution of the Archean Hope Bay greenstone belt, Nunavut, Canada; MSc thesis, University of British Columbia, Vancouver, British Columbia, 200 p.

**Sherlock, R.L. Carpenter, R.L., and Quang, C.**

2003: Volcanic stratigraphy, structural geology, and gold mineralization in the Wolverine-Doris Corridor, northern Hope Bay volcanic belt, Nunavut; Geological Survey of Canada, Current Research 2003-C7, 11 p.

**Sherlock, R.L. and Sandeman, H.A.**

2004: Volcanic stratigraphy and structural geology of the Boston area, Hope Bay volcanic belt, Nunavut; Geological Survey of Canada, Current Research 2004-C2, 11 p.

**Siivola, J. and Schmid, R.**

2007: A systematic nomenclature for metamorphic rocks: 12. List of mineral abbreviations. Recommendations by the IUGS Subcommittee on the Systematics of Metamorphic Rocks; Recommendations, web version of 01.02.2007.

**Stemler, J.U., Richards, J.P., and Muehlenbachs, K.**

2006: A fluid inclusion and stable isotopic investigation of the Boston lode-gold deposit, Hope Bay volcanic belt, Nunavut; *Exploration and Mining Geology* v. 15, p. 101-121.

**Sun, S.S. and McDonough, W.F.**

1989: Chemical and isotopic systematics of oceanic basalts: implications for mantle composition and processes, *in*. Saunders, A.D., and Norry, M.J., ed., *Magmatism in the Ocean Basins*; Geological Society Special Publication, v. 42, p. 313-345.

**Thompson, P.H.**

1997: Regional geology of Archean granitoid rocks adjacent to Hope Bay and Elu inlet volcanic belts, northeastern Slave structural province, Canadian Shield; BHP Minerals Canada Ltd., Internal Report, 56 p.



**Tomkins, A.G. and Grundy, C.**

2009: Upper temperature limits of orogenic gold deposit formation: constraints from the granulite-hosted Griffin's Find deposit, Yilgarn Craton; *Economic Geology*, v.104, 669-685.

**van Breemen, O., Thompson, P.H., Hunt, P.A., and Culshaw, N.**

1987: U-Pb zircon and monazite geochronology from the northern Thelon Tectonic Zone, District of Mackenzie; *in*. Radiogenic Age and Isotopic Studies, Report 1, Geological Survey of Canada, Paper 87-2, p. 81-93.

**Winchester, J.A. and Floyd, P.A.**

1976: Geochemical magma type discrimination. Application to altered and metamorphosed basic igneous rocks; *Earth and Planetary Science Letters*, v. 28, p. 459-469.

**Winchester, J.A. and Floyd, P.A.**

1977: Geochemical discrimination of different magma series and their differentiation products using immobile elements; *Chemical Geology*, v. 20, p. 325-343.

**Wonder, J., Spry, P., and Windom, K.**

1988: Geochemistry and origin of manganese-rich rocks related to iron-formation and sulfide deposits, western Georgia; *Economic Geology*, v.83, p. 1070-1081.

**Wood, D.A.**

1980, The application of a Th-Hf-Ta diagram to problems of tectonomagmatic classification and to establishing the nature of crustal contamination of basaltic lavas of the British Tertiary volcanic province; *Earth and Planetary Science Letters*, v. 50, p. 11-30.

### ***Figure captions***

Figure 1: a) Bedrock geological map of the Slave Craton (SC) with inset showing SC location within the Canadian Shield (modified after Hoffman and Hall, 1993; Bleeker et al., 1999; Stubbley, 2005; Shannon, 2008). b) Geological map of Archean granitoids associated with Hope Bay and Elu belts (after Thompson, 1997). Inset shows location of the studied area.

Figure 2: Superposed geological and water system maps in the Elu Link. b) Geological map and strain trajectories of the Elu Link. The greenstones form discontinuous small belts bounded by felsic meta-igneous rocks. c-d) Representative cross sections showing sheet-like meta-igneous intrusive bodies within tight to open, variably vergent folds of metavolcanic rocks. The sheet-like intrusive bodies are intensively interleaved with layers of metavolcanic rocks on their margins. Note foliation boudinage structures in both map and cross section views.

Figure 3: Correlation between Flake Lake (a) (Shannon, 2008) and Elu Link (b) stratigraphic columns. Note the absence of the migmatitic orthogneiss and the metagranite intrusions in the Flake Lake area.

Figure 4: Contact relationships between EL main rock units. a+b) Stretched and pulled apart metamafic enclaves in syn-D<sub>2</sub> amphibole ± biotite metagranite (a: UTM 13W, 457080E, 7520030N; b: UTM 13W, 457441E, 7519597N). c) Knife-sharp contact between amphibole ± biotite metagabbro (earlier) and amphibole ± biotite metagranite (later); UTM 13W, 451912E, 7515136N. d) Enclaves of two (1+2) crosscutting pre- to syn-D<sub>1</sub> mafic intrusions, cut by leucosome veins in syn-D<sub>2</sub> amphibole ± biotite metagranite; UTM 13W, 456948E, 7520348N.

Figure 5: Photomicrographs showing typical textural relationships of the rock-forming minerals. a) Metapsammite with chlorite<sub>1</sub> and Chlorite<sub>2</sub> representing crenulated S<sub>0</sub>/S<sub>1</sub> foliation and S<sub>2</sub> axial planar cleavage, respectively; UTM 13W, 444813E, 7508735N. b) Felsic metavolcanic rock showing two generations of garnet<sub>1</sub> (poikiloblastic cores) and garnet<sub>2</sub> (inclusion-free rims and blasts) in plane-polarized light; UTM 13W, 451059E, 7514976N. Note the textural equilibrium between Grt<sub>2</sub> and Bt. c) albite<sub>1</sub> porphyroclast mantled by recrystallized fine-grained matrix of amphibole and albite<sub>2</sub> in mafic metavolcanic rocks; UTM 13W, 451267E, 7514389N. d) Quartz and feldspar porphyroclasts surrounded by a fine-grained quartzofeldspathic mosaic in amphibole ± biotite metagranite; UTM 13W, 449505E, 7512822N. e) Strain-free chlorite-rich retromorphic assemblage derived from magmatic minerals in a dolerite; e) Non-deformed dolerite dike depicting relics of the magmatic assemblage amphibole + plagioclase ± magnetite in a matrix of chlorite dominated retromorphic assemblage; UTM 13W, 463117E, 7525806N. Figs. 5a + 5c-e in cross-polarized light. Abbreviations after Siivola and Schmid (2007).

Figure 6: Classification of EL mafic meta-igneous rocks using the diagrams a) Nb/Y vs. Zr/TiO<sub>2</sub>. b) Zr/P<sub>2</sub>O<sub>5</sub> vs. TiO<sub>2</sub>, and c+d) TiO<sub>2</sub> vs. Al<sub>2</sub>O<sub>3</sub> (mafic metavolcanic rocks in (c) and metagabbro in (d)). Fields in (a+b) are after Winchester and Floyd (1976, 1977).

Figure 7: Chondrite- and N-MORB-normalized plots of the mafic meta-igneous rocks distinguished into four magmatic sub-suites.

Figure 8: Tectonic setting discrimination of the mafic meta-igneous rocks using the diagrams a) Ti vs. V (Shervais, 1982), b) Zr-Ti-Y (Pearce and Cann, 1973), and d) Th-Hf-Ta (Wood et al., 1980).

Figure 9: Geochemical characteristics of the EL felsic meta-igneous rocks. a) classification using the diagram Nb/Y vs Zr/TiO<sub>2</sub> (Winchester and Floyd, 1976). b) Hf-Zr plot. c) chondrite-normalized plot, d) ORG-normalized plot.

Figure 10: Tectonic setting discrimination of the felsic meta-igneous rocks using Y vs. Nb (a), Y+Nb vs. Rb (b), Yb vs. Ta (c), and (d) Yb+Ta vs. Rb bivariate diagrams of Pearce et al. (1984). Delimited oval field is that of the Flake Lake felsic suite. Symbols as in Fig. 9b.

Figure 11: Outcrop-scale folds and deformation phases in Elu Link. a) F<sub>2</sub> folds folding a penetrative bedding parallel S<sub>0</sub>/S<sub>1</sub> foliation in the metavolcanic rocks; UTM 13W, 452675E, 7514450N. b) F<sub>2</sub> folds of S<sub>1</sub> foliation in the mafic veined gneiss; UTM 13W, 456148E, 7517723N. c+d) Intrafolial buckled folds nucleated around pillow lavas (in dark grey) and illustrating competence contrast between the intrusive bodies (stippled) and their host metavolcanic rocks during D<sub>3</sub> deformation; UTM 13W, 447500E, 7515075N. In light grey are quartz veins.

Figure 12: Lower hemisphere equal area projection of structural elements. Poles to S<sub>0</sub>/S<sub>1</sub> (a+e+i) and S<sub>2</sub> (b+f+j) foliations show a radial stereonet distribution consistent with boudinaged large-scale tight F<sub>2</sub> folds. L<sub>2</sub> stretching lineation (c+g+k) and F<sub>2</sub> fold axes (d+h+l). Note that L<sub>2</sub> + F<sub>2</sub> are coaxial and radial suggesting D<sub>2</sub> domal structures. Small black squares represent average values. Contours interval is 2%.

Figure 13: Outcrop attributes and geometry of D<sub>2</sub> shear zones in the Elu Link. a) Conjugate shear bands with injected leucosomes in amphibole ± biotite metagranite; UTM 13W, 453813E, 7517547N. b) Thrust zone (dip = ~ 30 °) filled with quartz veins in amphibole ± biotite metagabbro; UTM 13W, 447855E, 7516060N. c) Conjugate shear bands precursor of carbonate alteration zones in amphibole ± biotite metagabbro; UTM 13W, 447574E, 7515359N. d) Reverse conjugate strike-slip shear zones due to D<sub>3</sub> overprinting of D<sub>2</sub> structures; UTM 13W, 448475E, 7515230N.

Figure 14: Alteration map of the Elu Link

Figure 15: Photomicrographs illustrating textural generations of sulfides. a-c) The first generations of sulfides crystallized along  $F_1$  microfolds, the second parallel to  $S_2$  axial cleavage, and the third forms euhedral blasts lacking any shape-preferred orientation in the metapsammite; UTM 13W, 444813E, 7508735N. d) Garnet porphyroblast showing inclusions of Ilmenite<sub>1</sub> and zircon<sub>1</sub> in the felsic metavolcanic rocks; UTM 13W, 451059E, 7514976N. e) Pyrite<sub>3</sub> blasts showing an inclusion of chalcopyrite hosting an early-formed pyrrhothite crystal; same location as in a-c+e. f) Pyrite<sub>3</sub> containing inclusions of early-formed pyrrhothite. Mineral abbreviations after Siivola and Schmid, 2007.

Figure 16:  $TiO_2$  vs. Zn plots showing positive correlation in the mafic metavolcanic rocks (a) and the metagabbros (b). Au vs. Cu plots in the mafic metavolcanic rocks (c), the metagabbros (d), and the metagranites and the dolerites (e). Note the relative abundance of Au in the metagabbros.

Figure 17: Anomalous concentration map of Au (> 1 ppb)

Figure 18: Anomalous concentration map of As (> 1 ppm)

Figure 19: Anomalous concentration map of Cu (> 100 ppm)

Figure 20: Anomalous concentration map of Zn (> 100 ppm)

## **APPENDIX**

### ***Analytical methods***

Magnetic susceptibility was measured on hand samples using a KT-10 magnetic susceptibility meter. Petrographic data were obtained from the study of polished thin sections and XRD analysis of samples using University of New Brunswick's Bruker D8 Advance Spectrometer. Geochemical analysis of 81 samples was performed by Newmont Mining in a commercial laboratory (ACME) in Vancouver using Inductively Coupled Plasma emission Spectrometry (ICP-MS). Internal standards to ACME laboratory were used. In order to check the quality of these data, a set of 42 samples was reanalyzed using the pressed pellet technique by Wavelength-Dispersive X-ray Fluorescence Spectrometry at Memorial University (see Longerich, 1995) and Instrumental Neutron Activation Analysis (INAA) analysis at Actlabs in Ontario. In both laboratories, MRG and MA-2C standards were used for quality data control. The results were recombined considering elements with the least absolute analytical error. To

minimize analytical errors in the determination of certain elements, XRF+INAA analyses were recombined with the ICP-MS data provided by Newmont Mining. Overall, both ICP-MS and recombined XRF+INAA datasets plot similarly allowing comparable interpretation. Because of their high number and for consistency with comparative HBB data, geochemical descriptions in this work are based only on the ICP-MS data provided by Newmont Mining. All datasets can be made available upon request.

### ***Tables***

Table 1: Mean and standard deviation of magnetic susceptibility data indicated by the EL rock units. n, number of measurements.

Table 2: Relationships between growth periods of metamorphic minerals and deformation phases.

Table 3: Mineral composition of the Elu Link main rock units.

Table 4: Average major and trace element concentrations by ICP-MS (1DX) (ACME) of the Elu Link rocks.

Table 5: Average major and trace element concentrations by ICP-MS (1DX) (ACME) of the Elu Link rocks. The complete raw geochemical dataset can be obtained from the GSC Canada-Nunavut Geological office database upon request.

Figure 1.

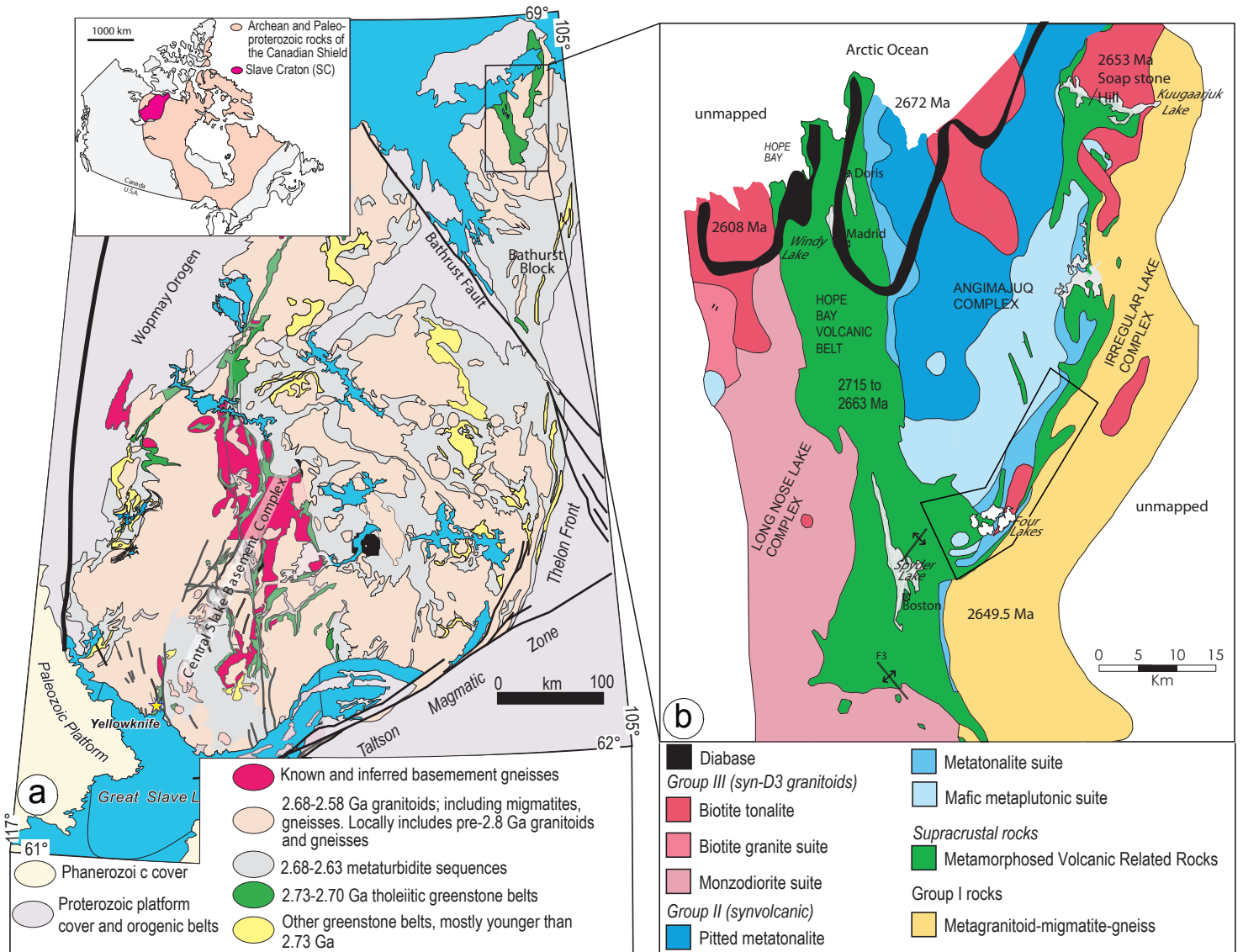


Figure 2a.

**Syn- to late-(D2+D3) rocks**

Moderately to weakly foliated phaneritic equigranular hornblende ± biotite metagranite

**Syn-D2 rocks**

Moderately foliated and magnetic porphyrophaneritic hornblende ± biotite metagranite

Porphyro-phaneritic, hornblende ± biotite metagabbros

**Pre- to syn-D1 rocks**

Migmatite-gneiss and associated leucosome veins (stippled)

Felsic metavolcanic rocks

Pillowed mafic metavolcanic rocks

Iron formation

Dolerites

Reverse shear zone (OSZ)

Thrust

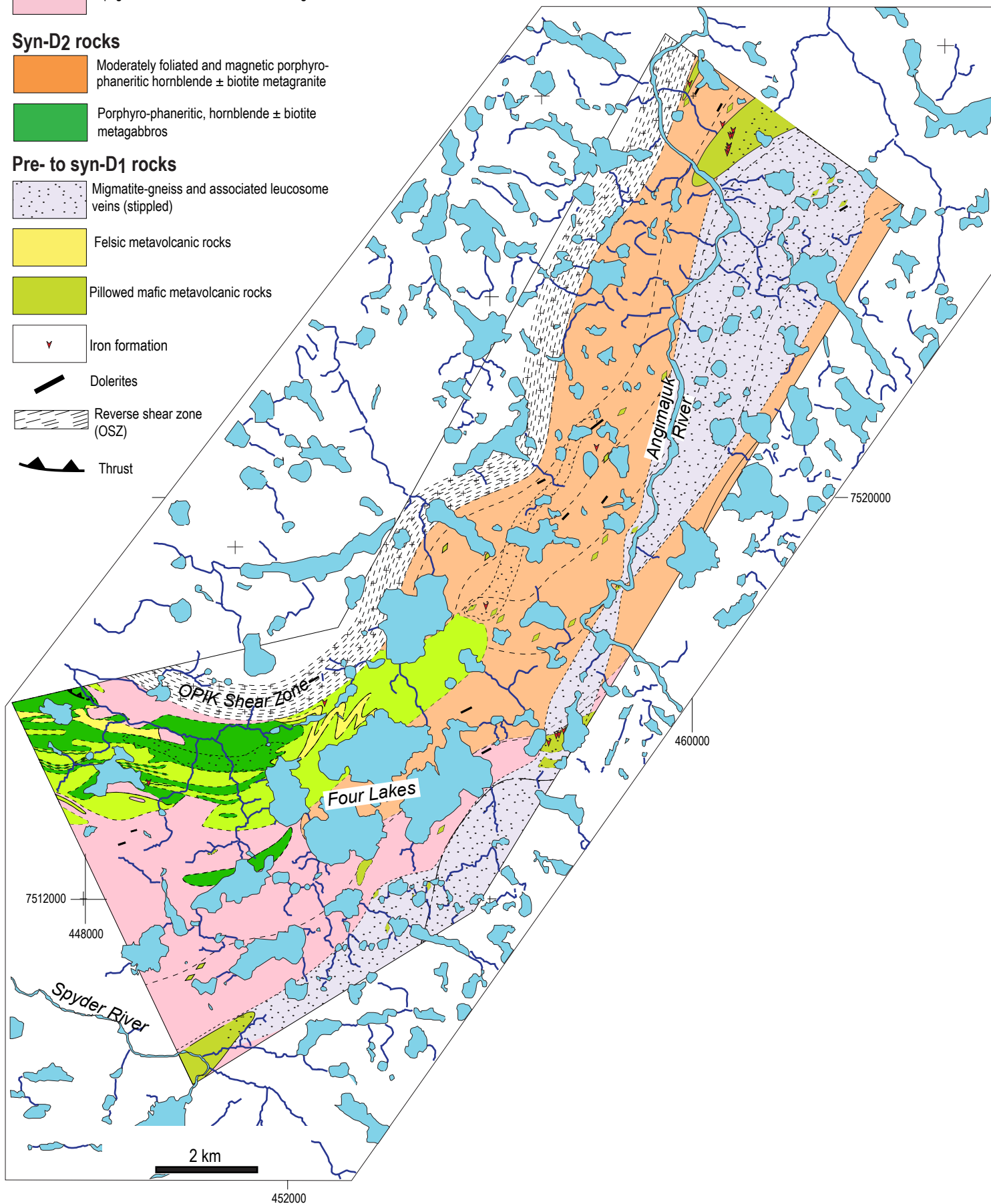


Figure 2 (continued).

**Syn- to late-(D2+D3) rocks**

Moderately to weakly foliated phaneritic equigranular hornblende ± biotite metagranite

**Syn-D2 rocks**

Moderately foliated and magnetic porphyrophaneritic hornblende ± biotite metagranite

Porphyro-phaneritic, hornblende ± biotite metagabbros



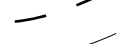

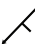
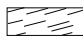

**Pre- to syn-D1 rocks**

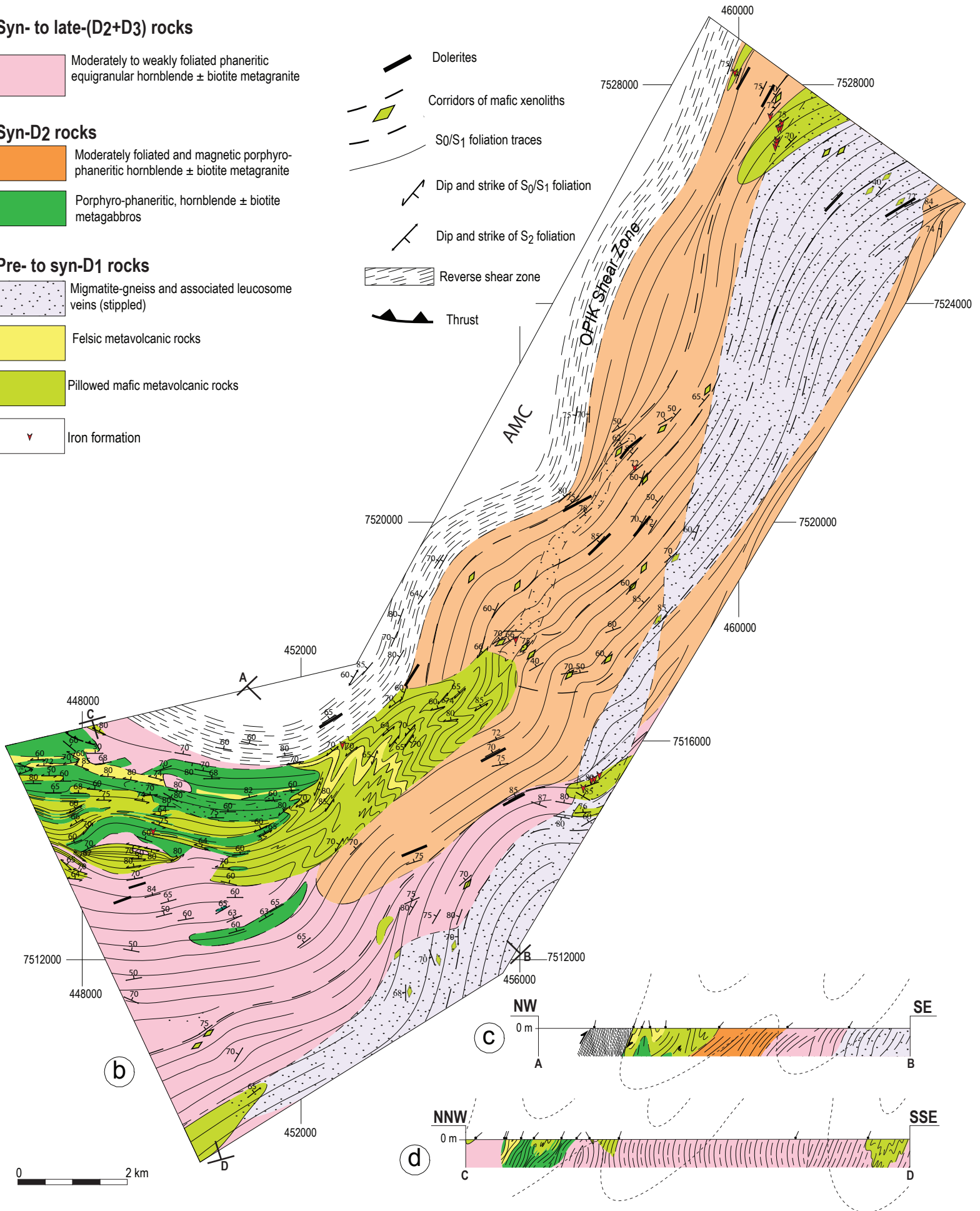
Migmatite-gneiss and associated leucosome veins (stippled)

Felsic metavolcanic rocks

Pillowed mafic metavolcanic rocks

Iron formation

-  Dolerites
-  Corridors of mafic xenoliths
-  S<sub>0</sub>/S<sub>1</sub> foliation traces
-  Dip and strike of S<sub>0</sub>/S<sub>1</sub> foliation
-  Dip and strike of S<sub>2</sub> foliation
-  Reverse shear zone
-  Thrust





**Figure 3.**

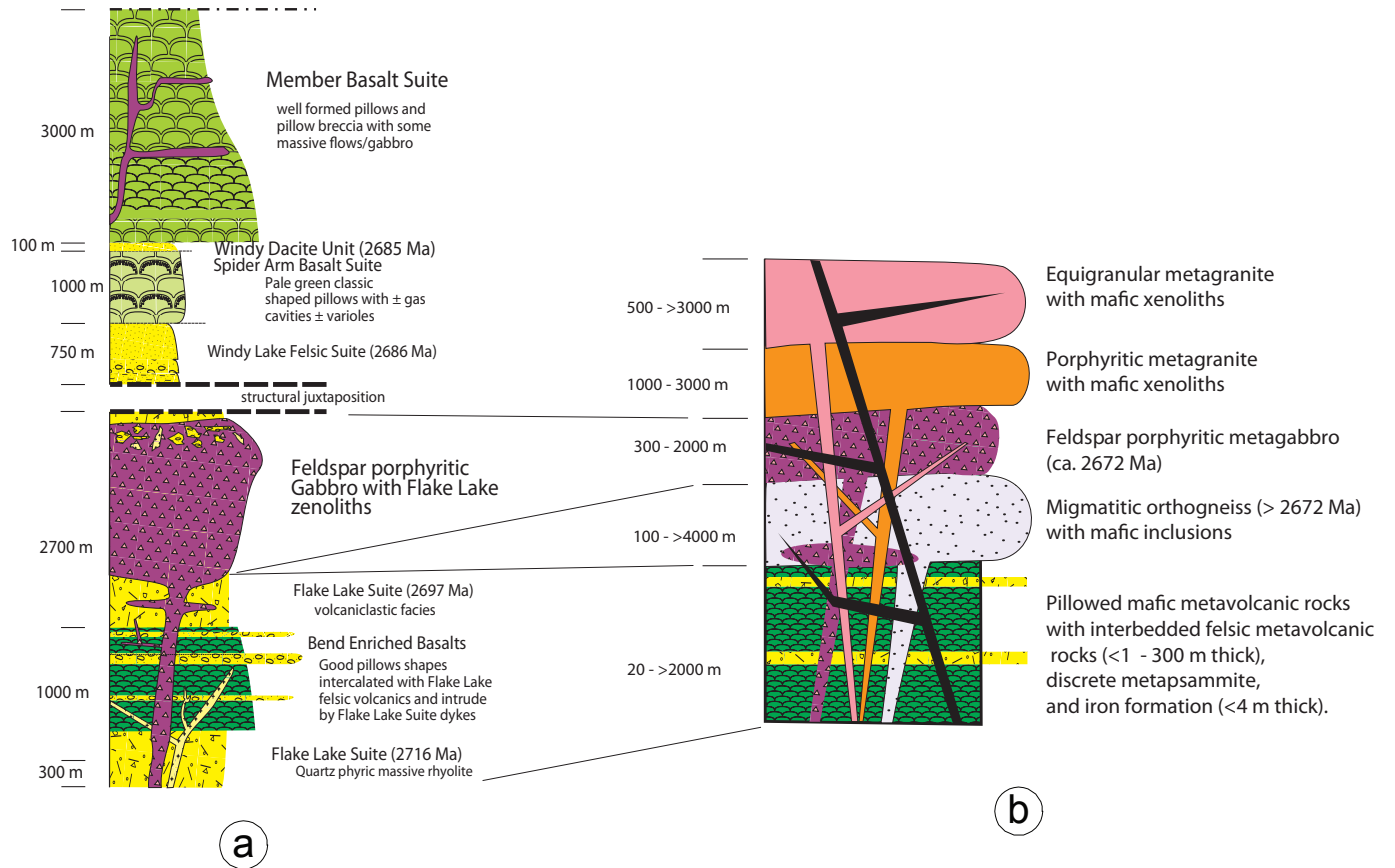


Figure 4.

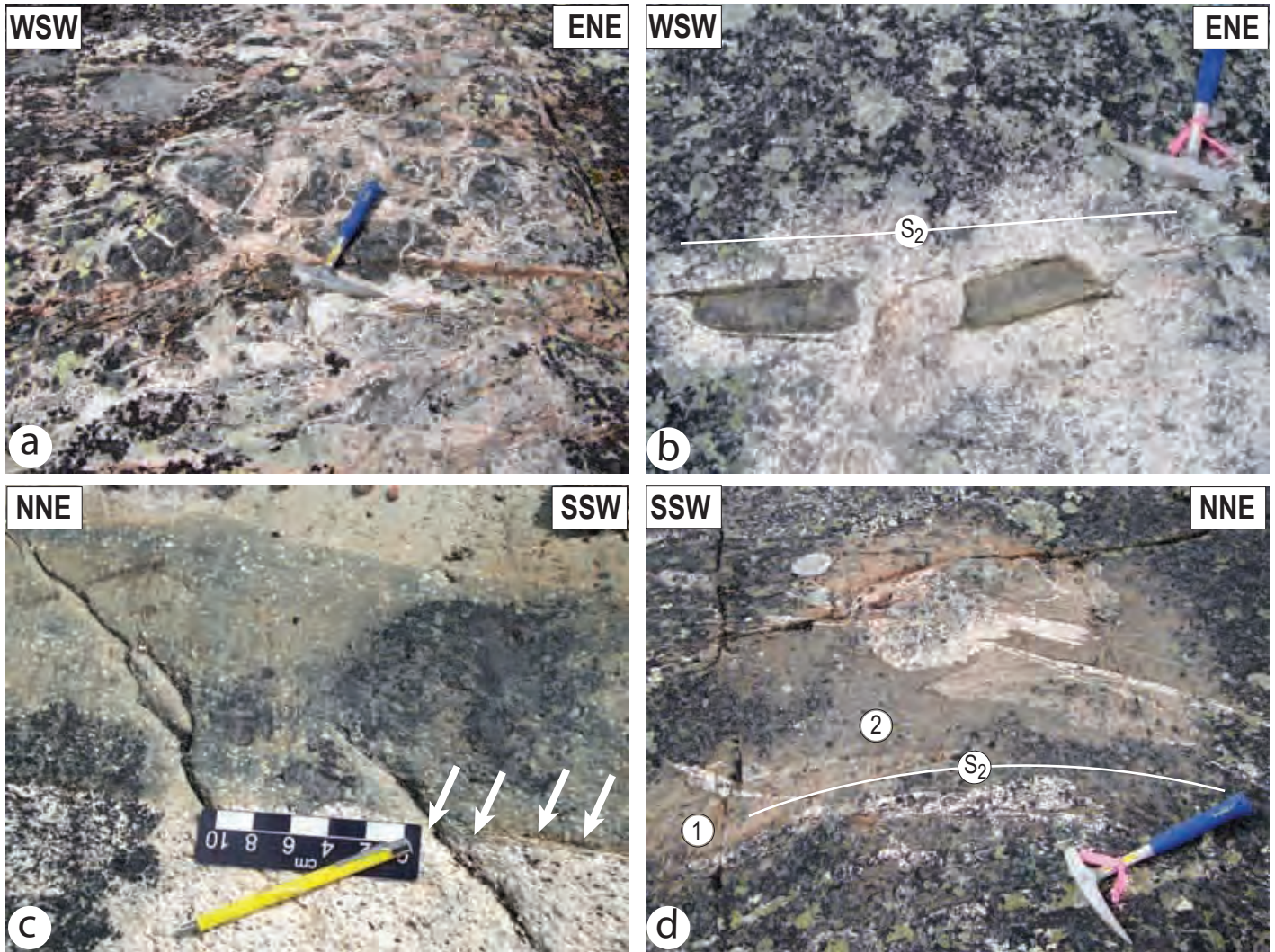




Figure 5.

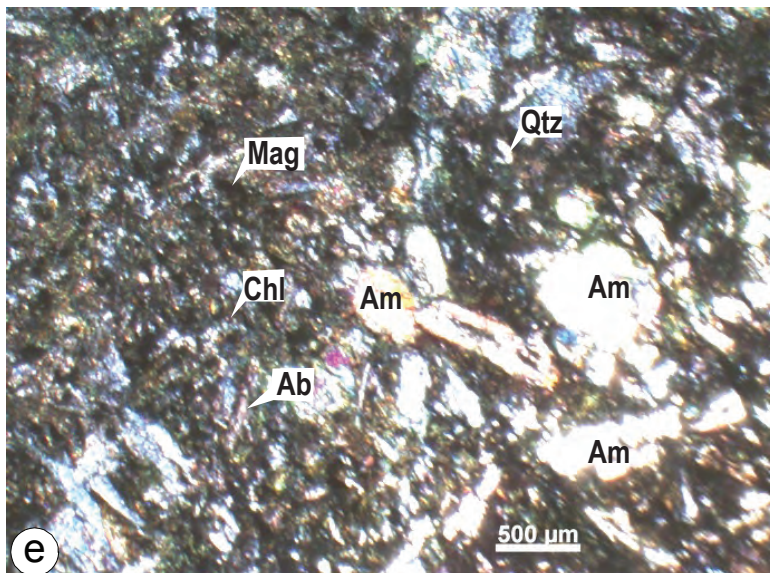
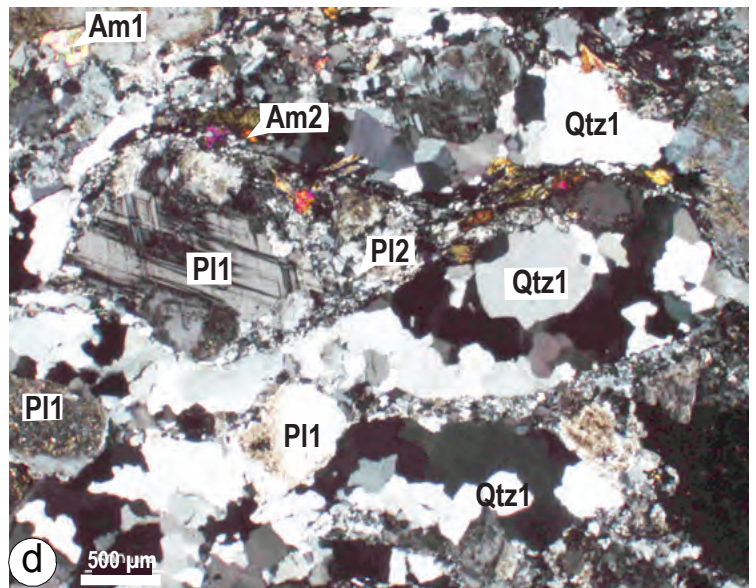
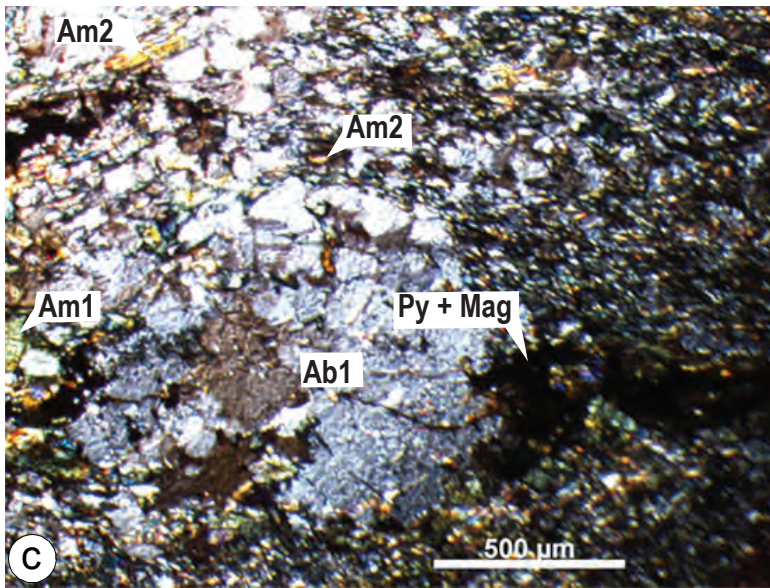
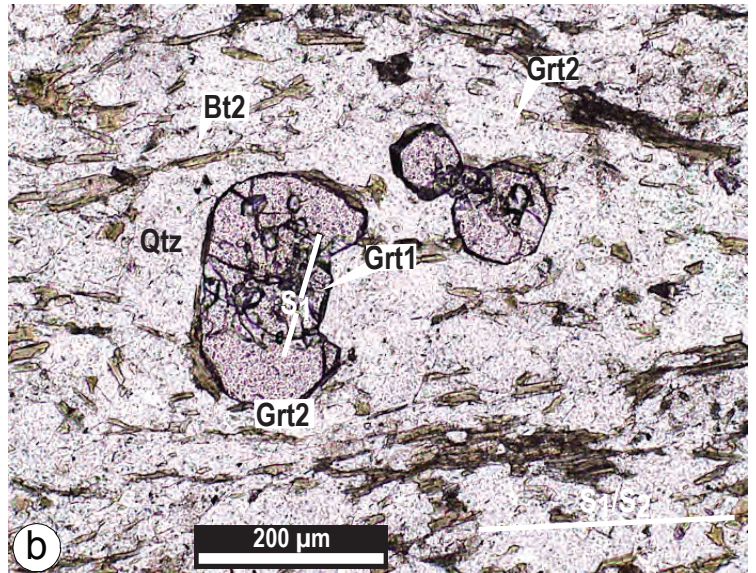
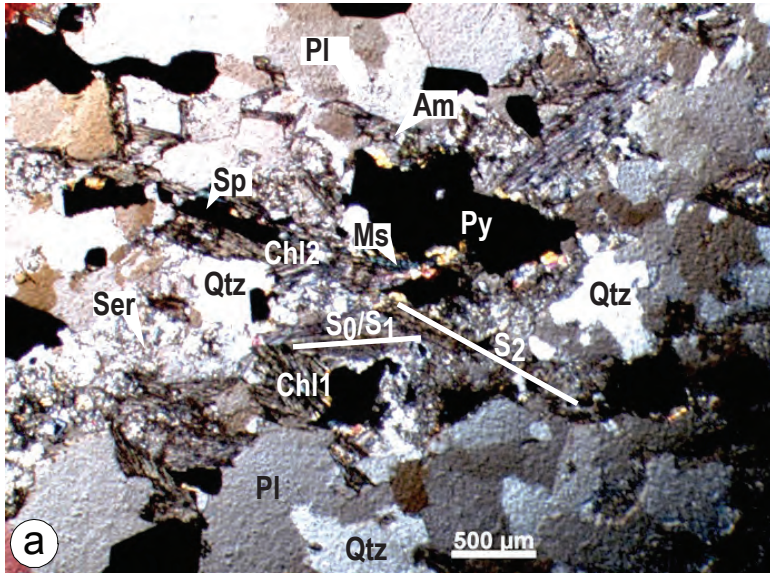




Figure 6.

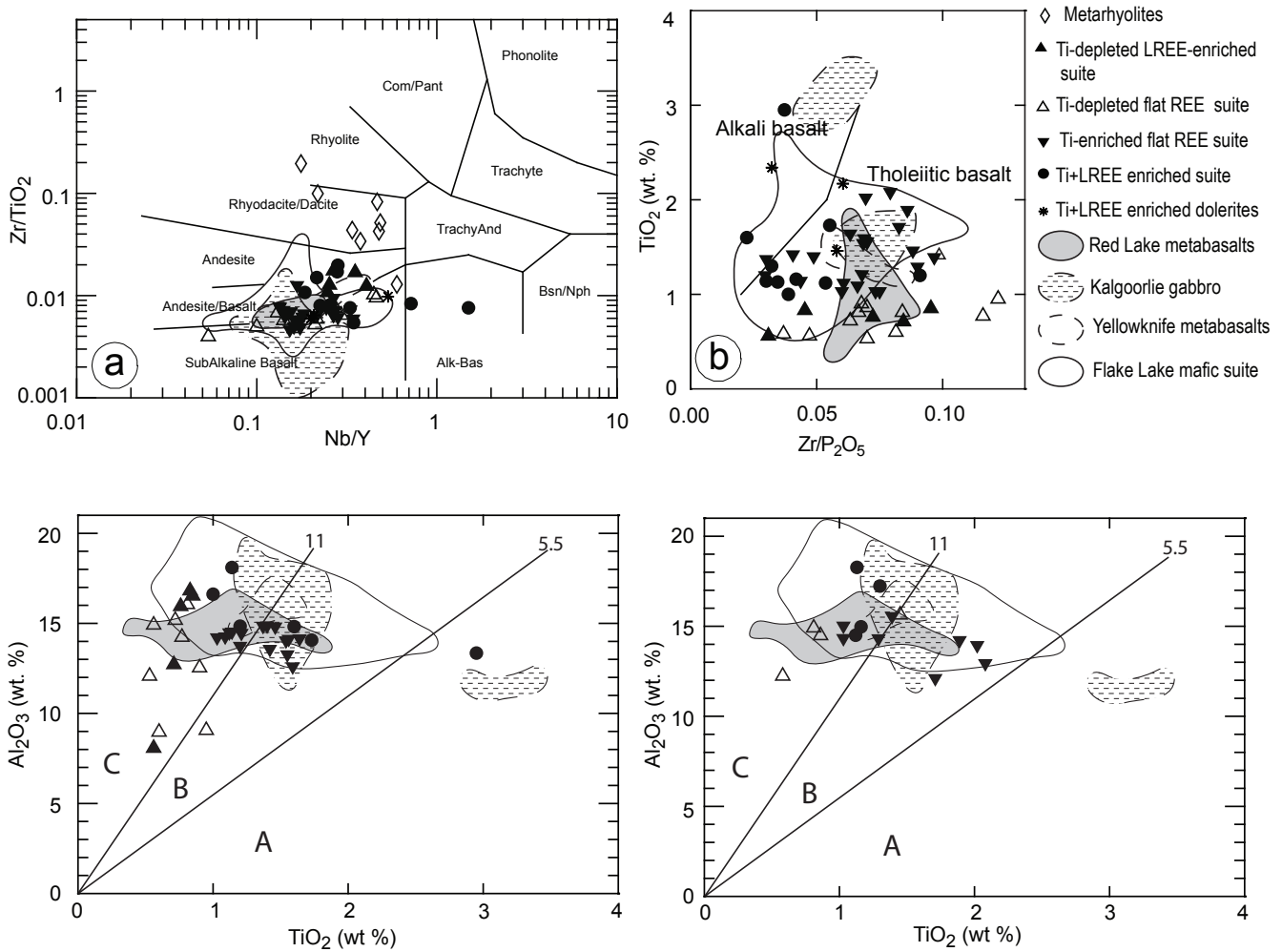


Figure 7.

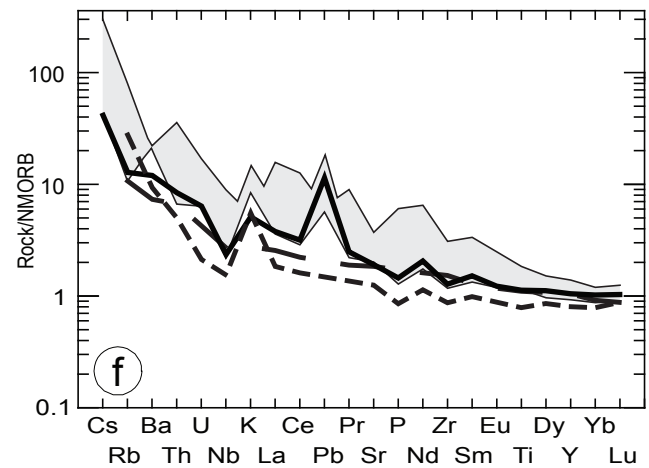
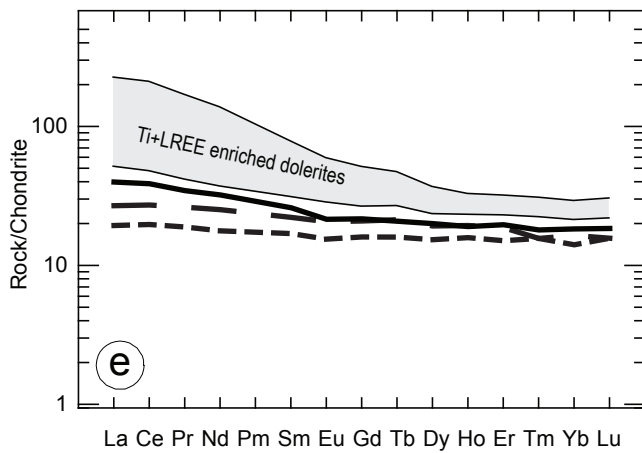
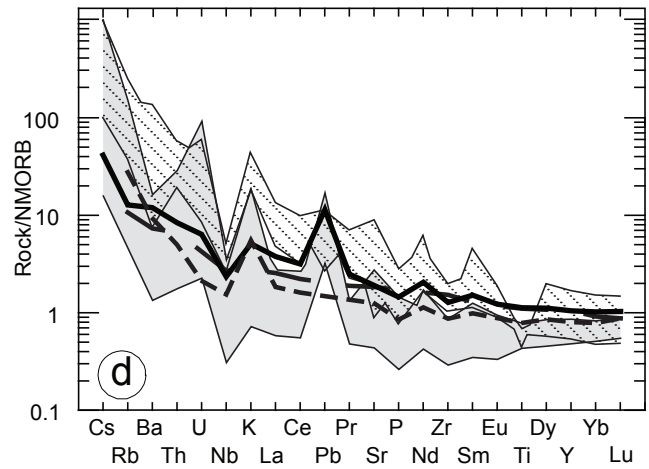
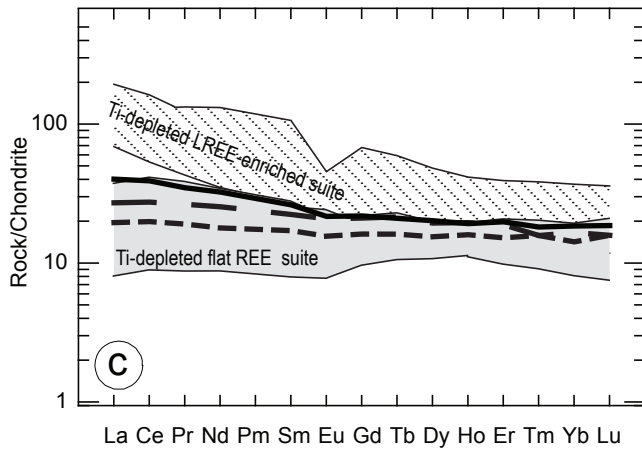
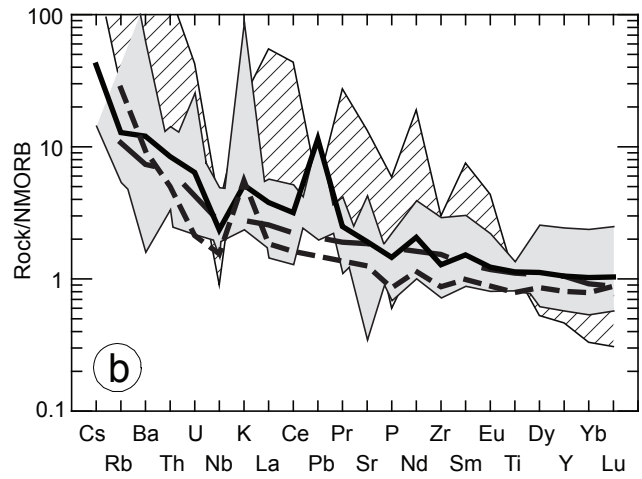
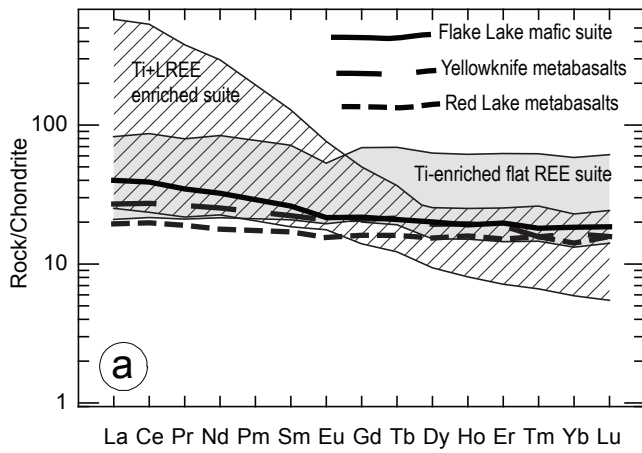
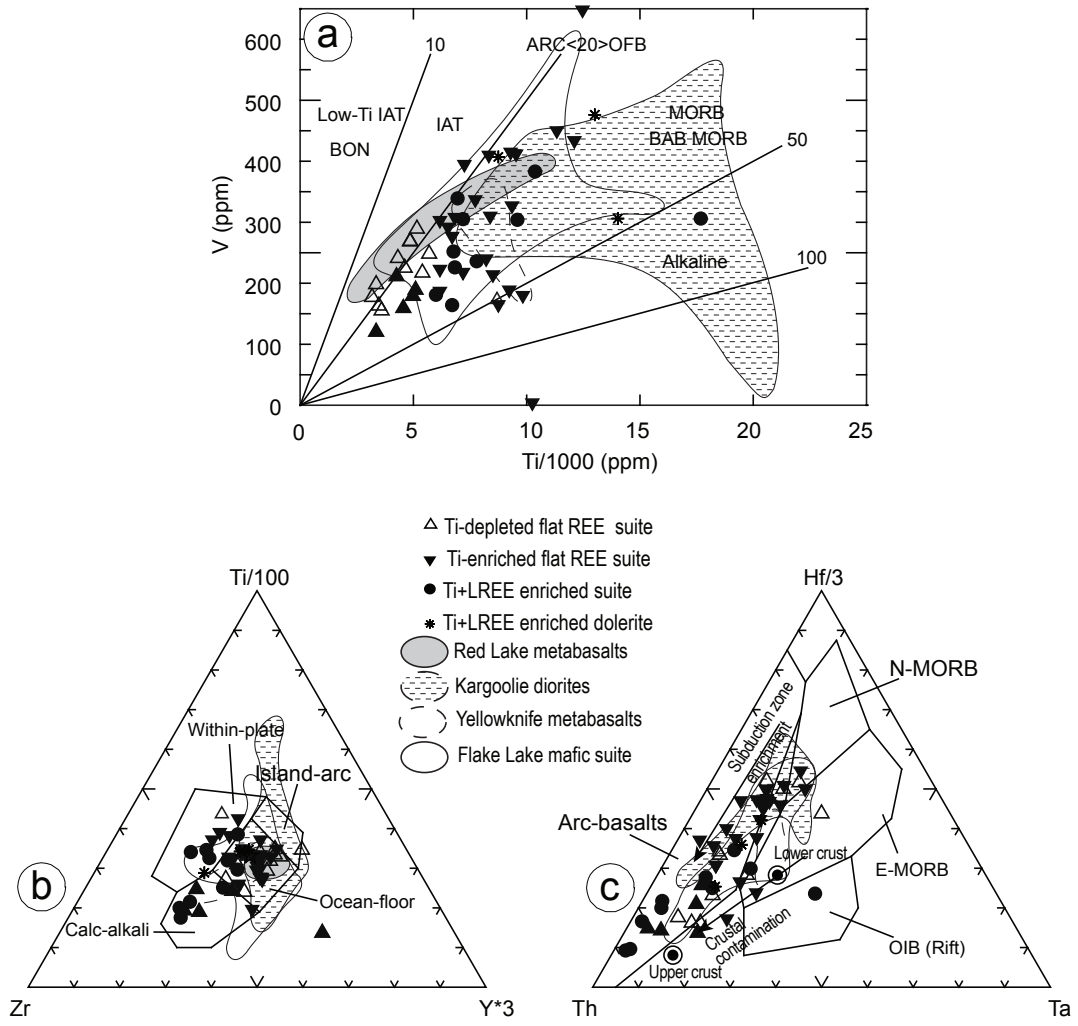


Figure 8.



**Figure 9.**

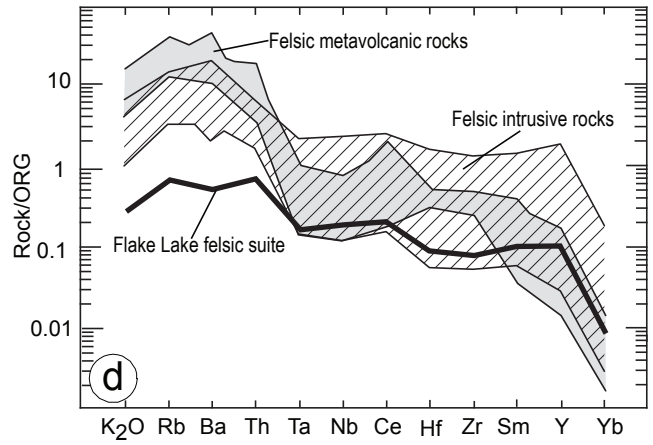
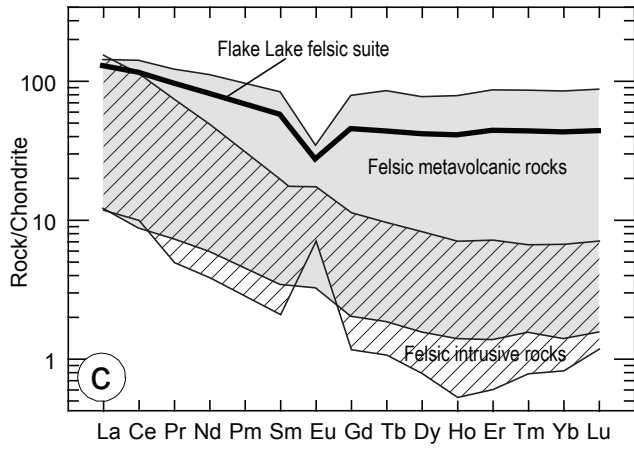
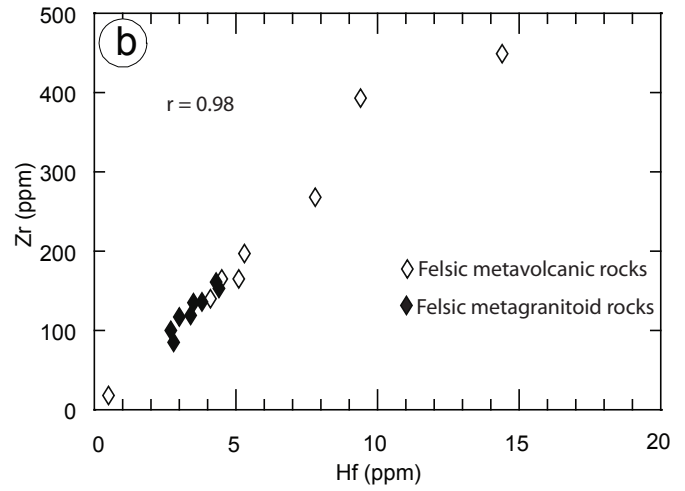
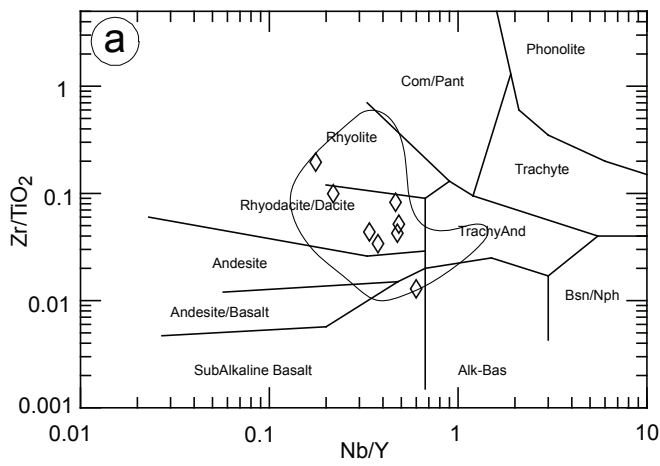


Figure 10.

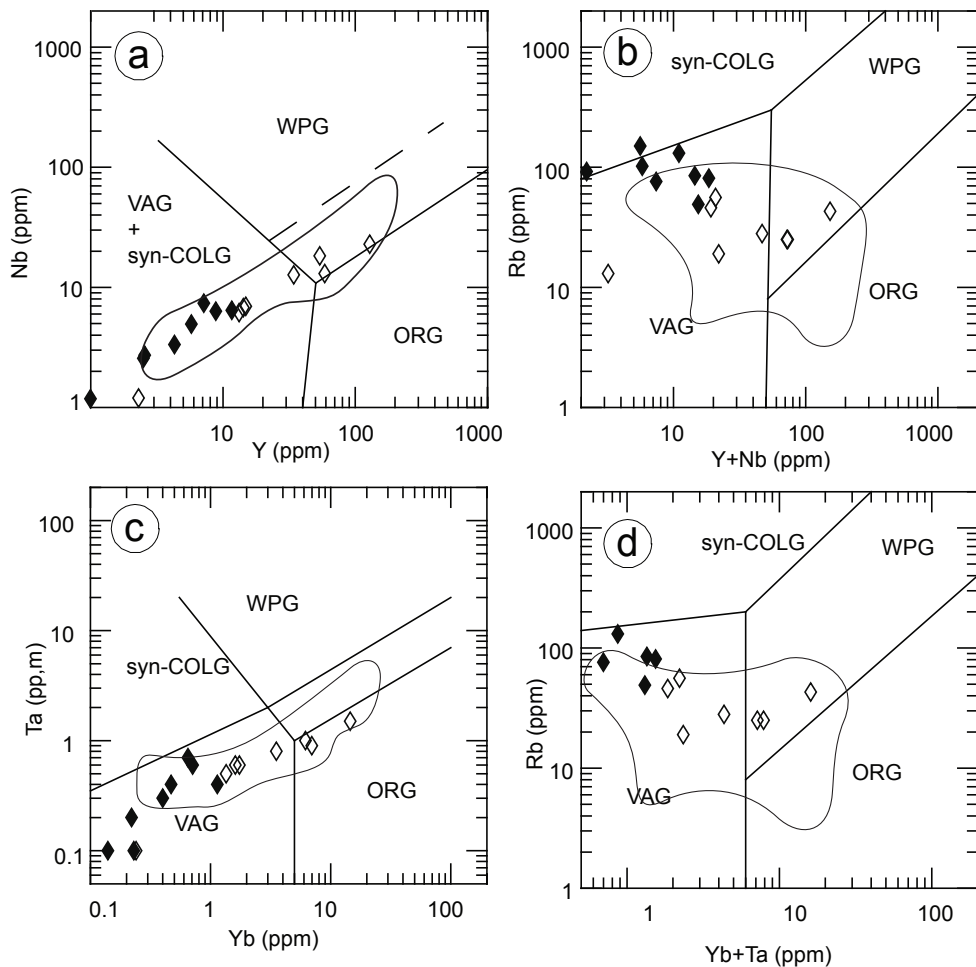




Figure 11.

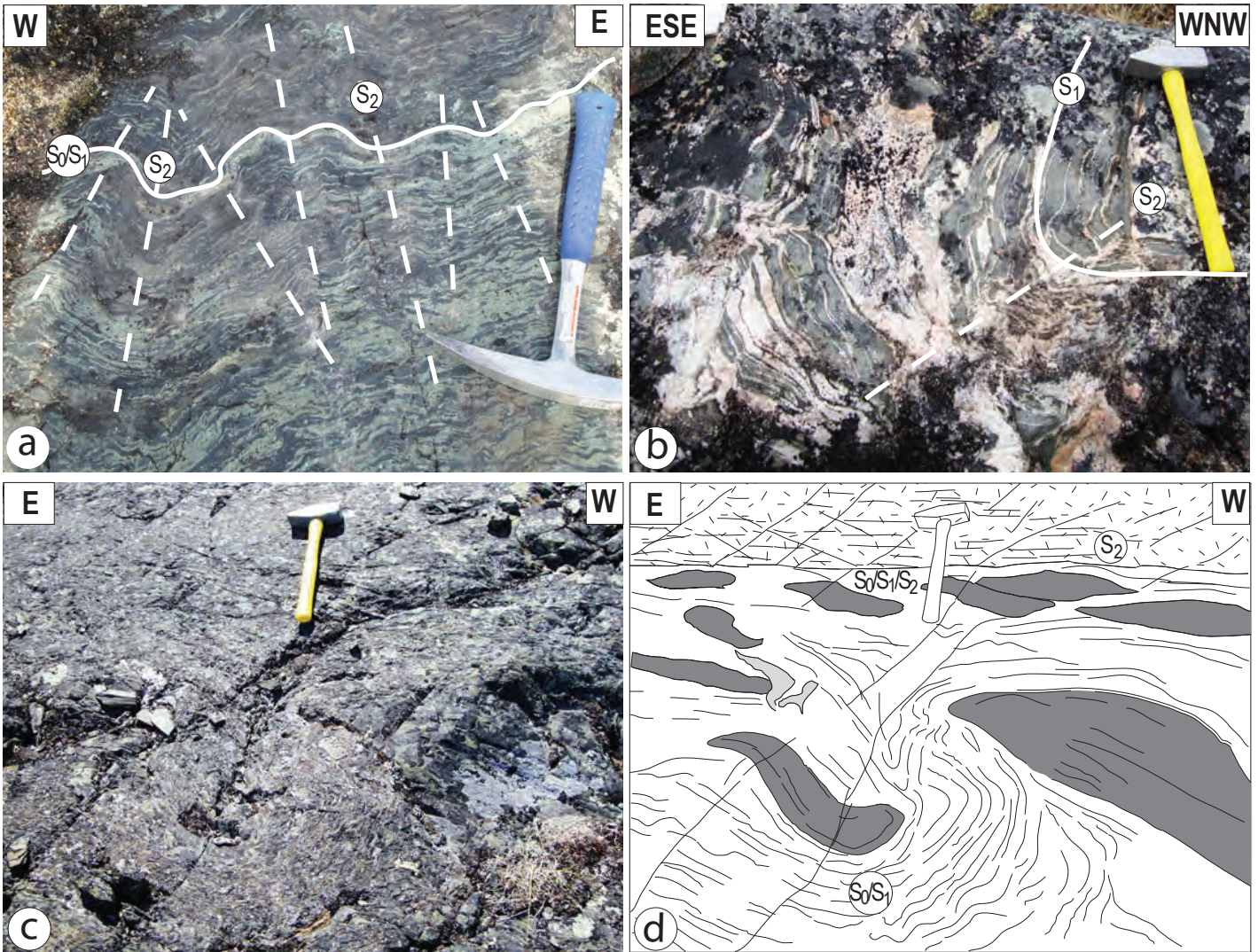


Figure 12.

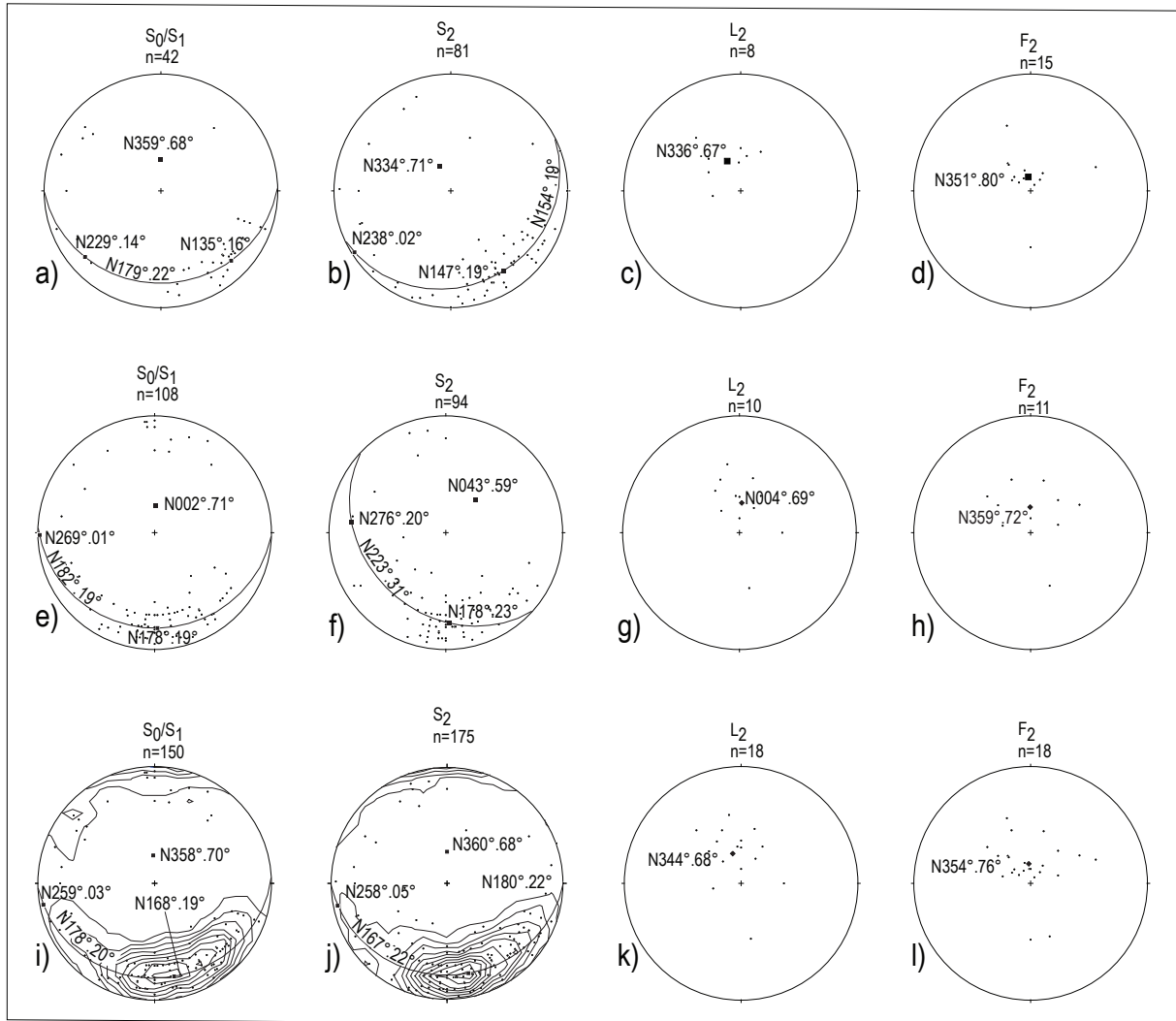




Figure 13.

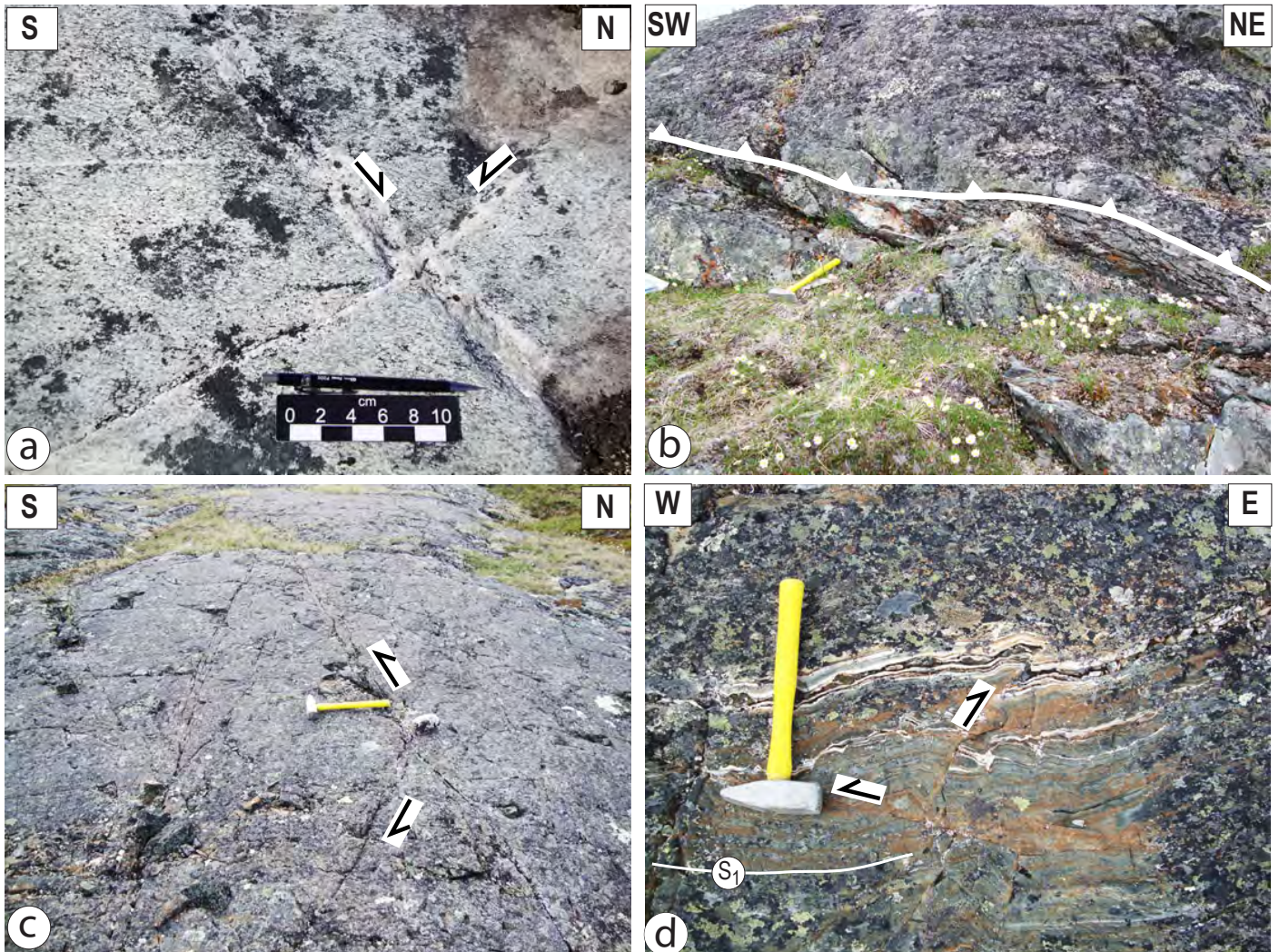


Figure 14.

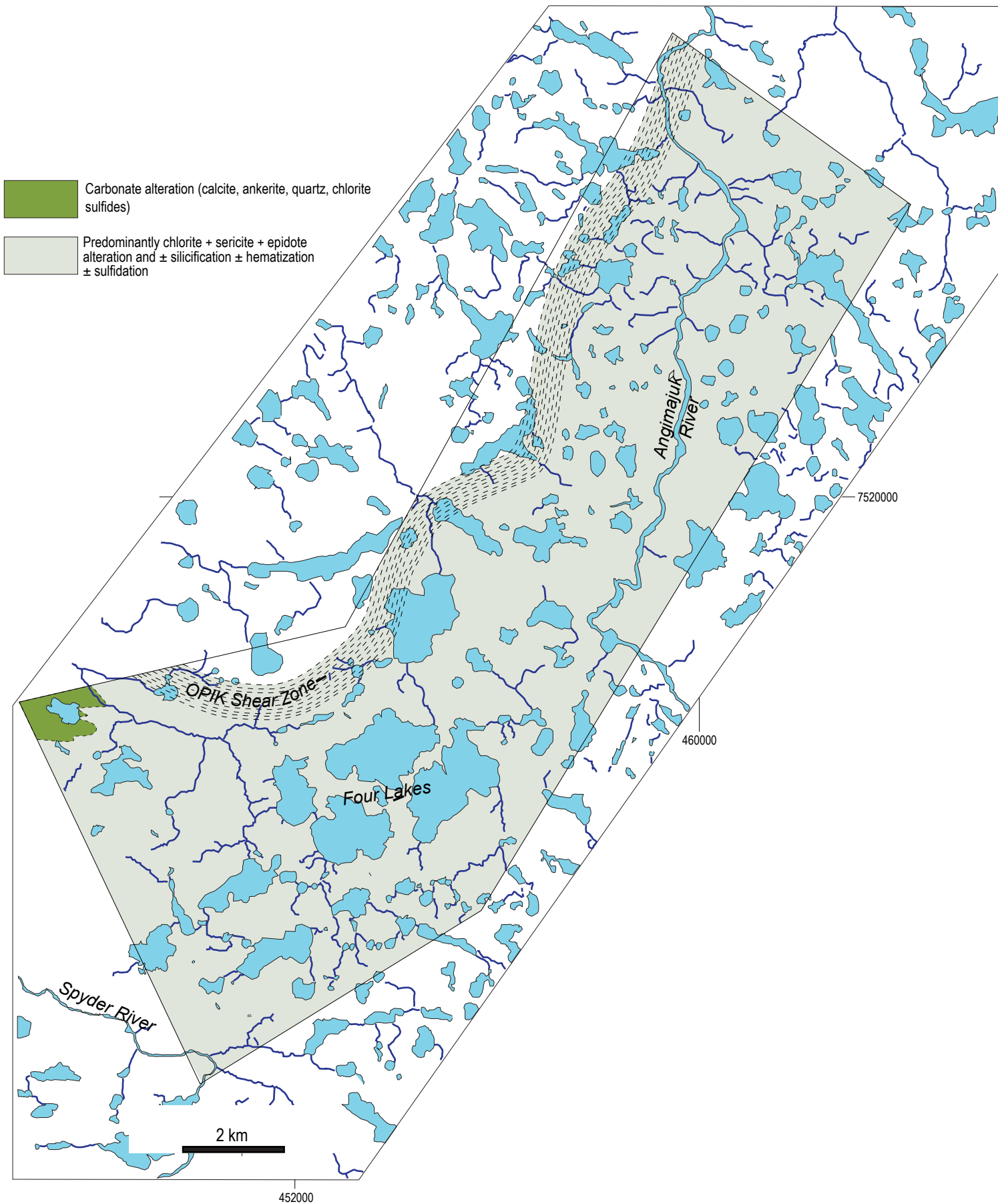




Figure 15.

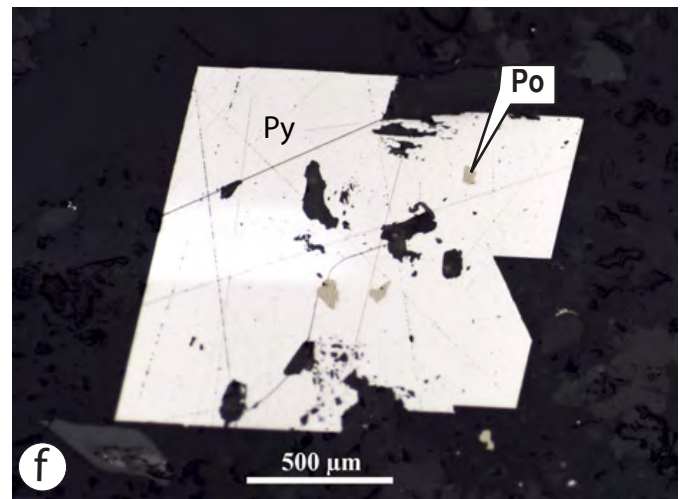
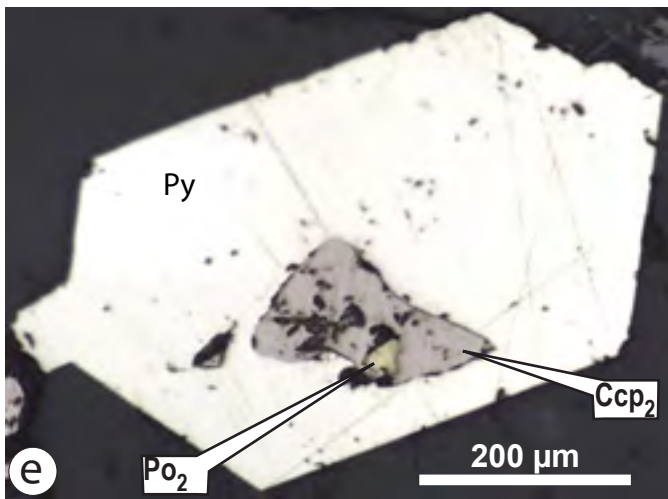
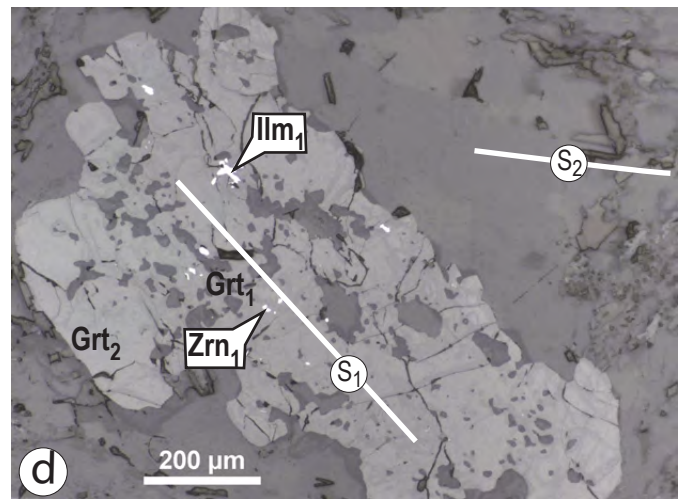
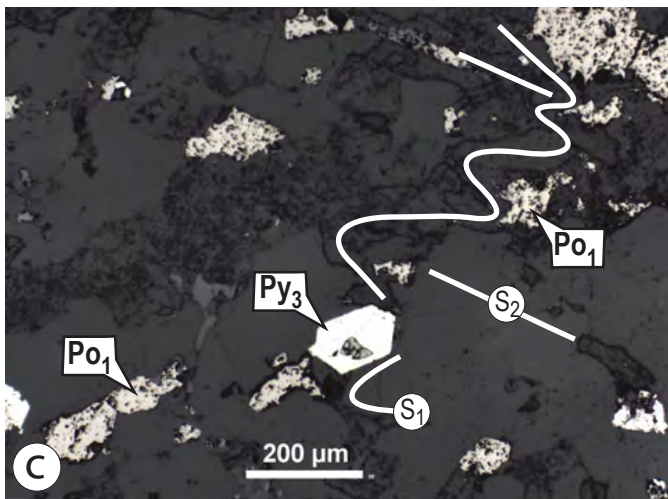
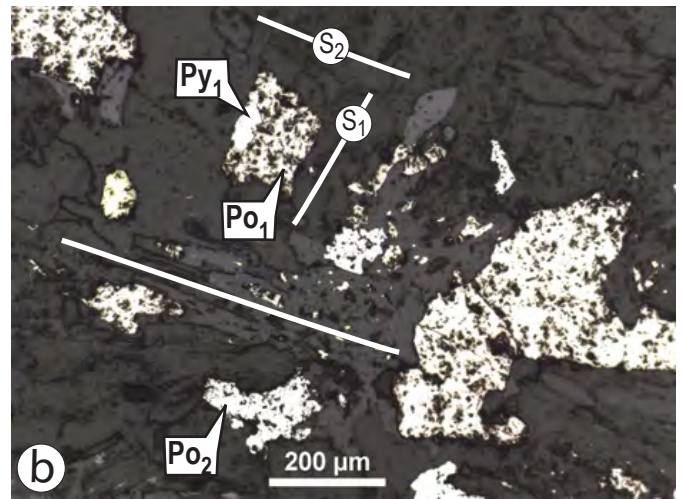
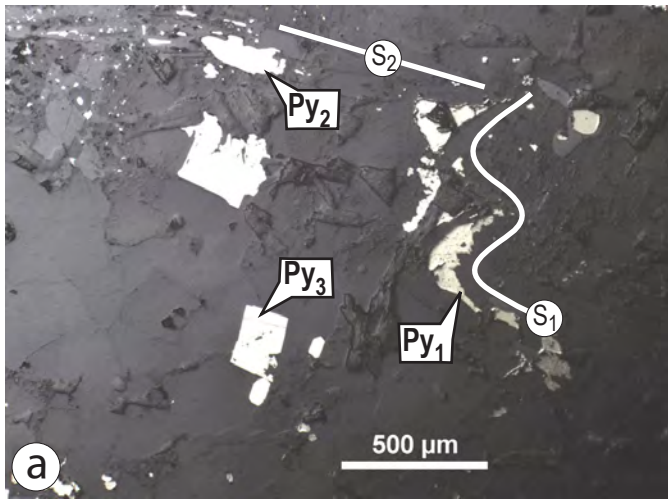


Figure 16.

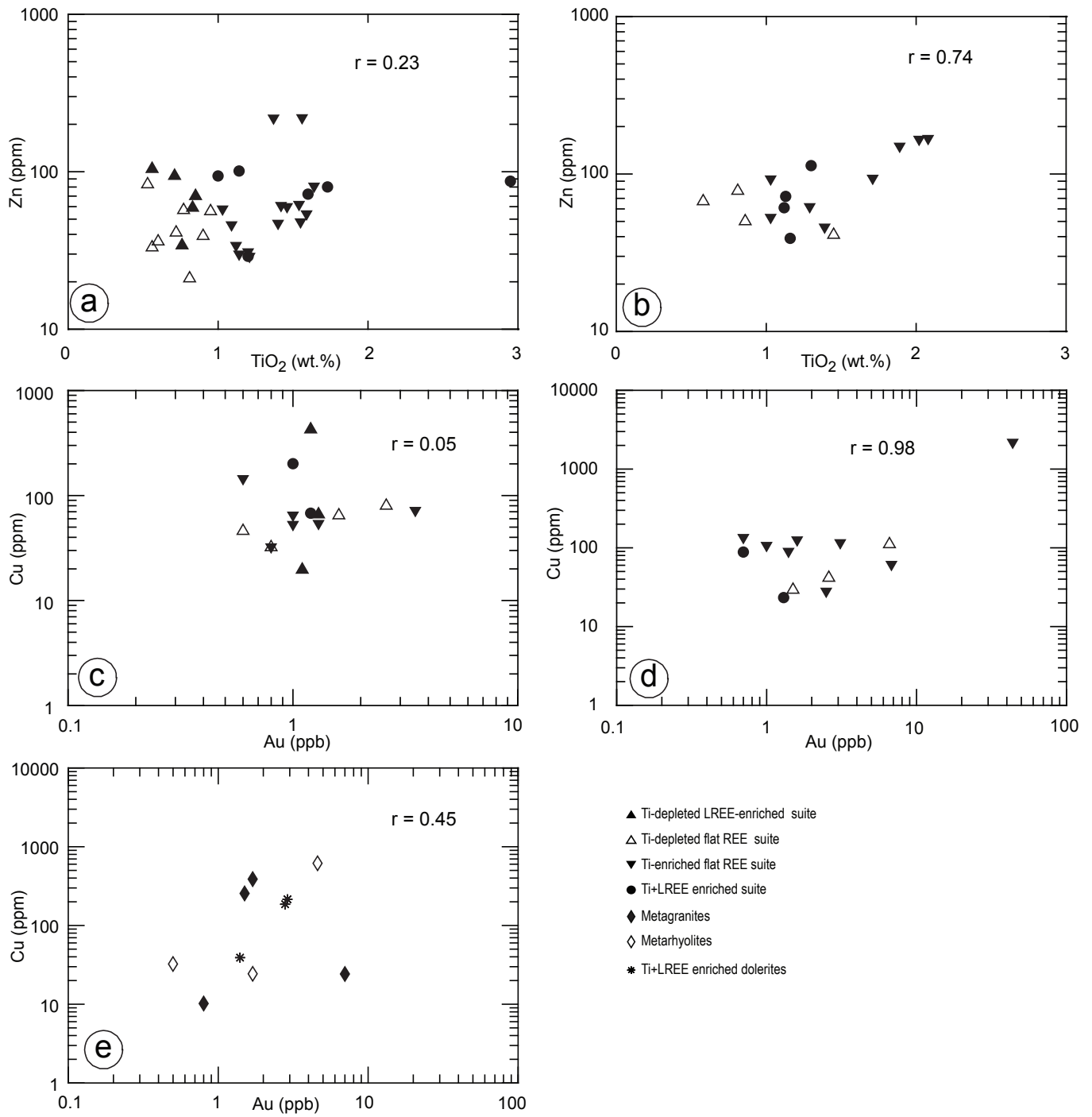




Figure 17.

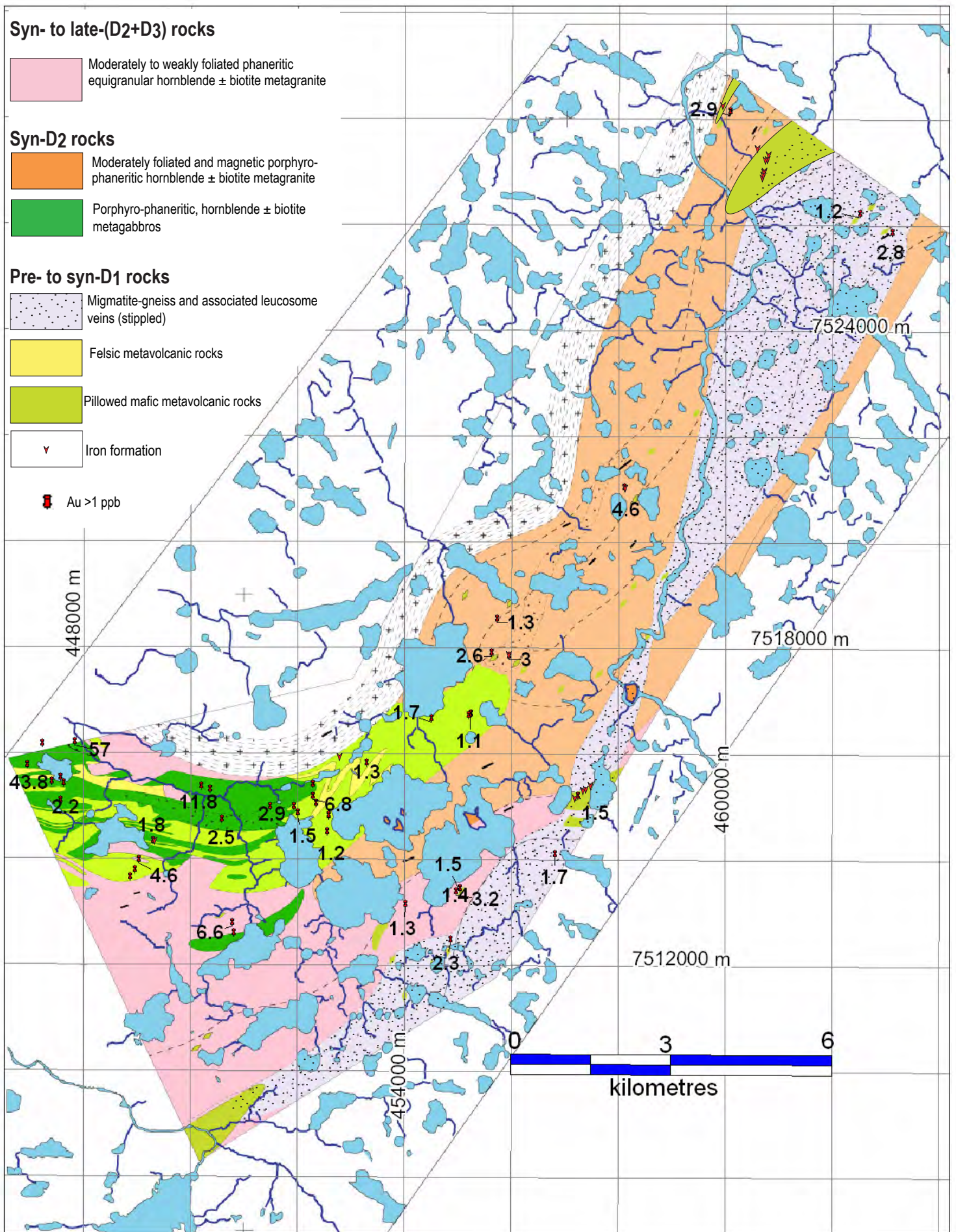




Figure 18.

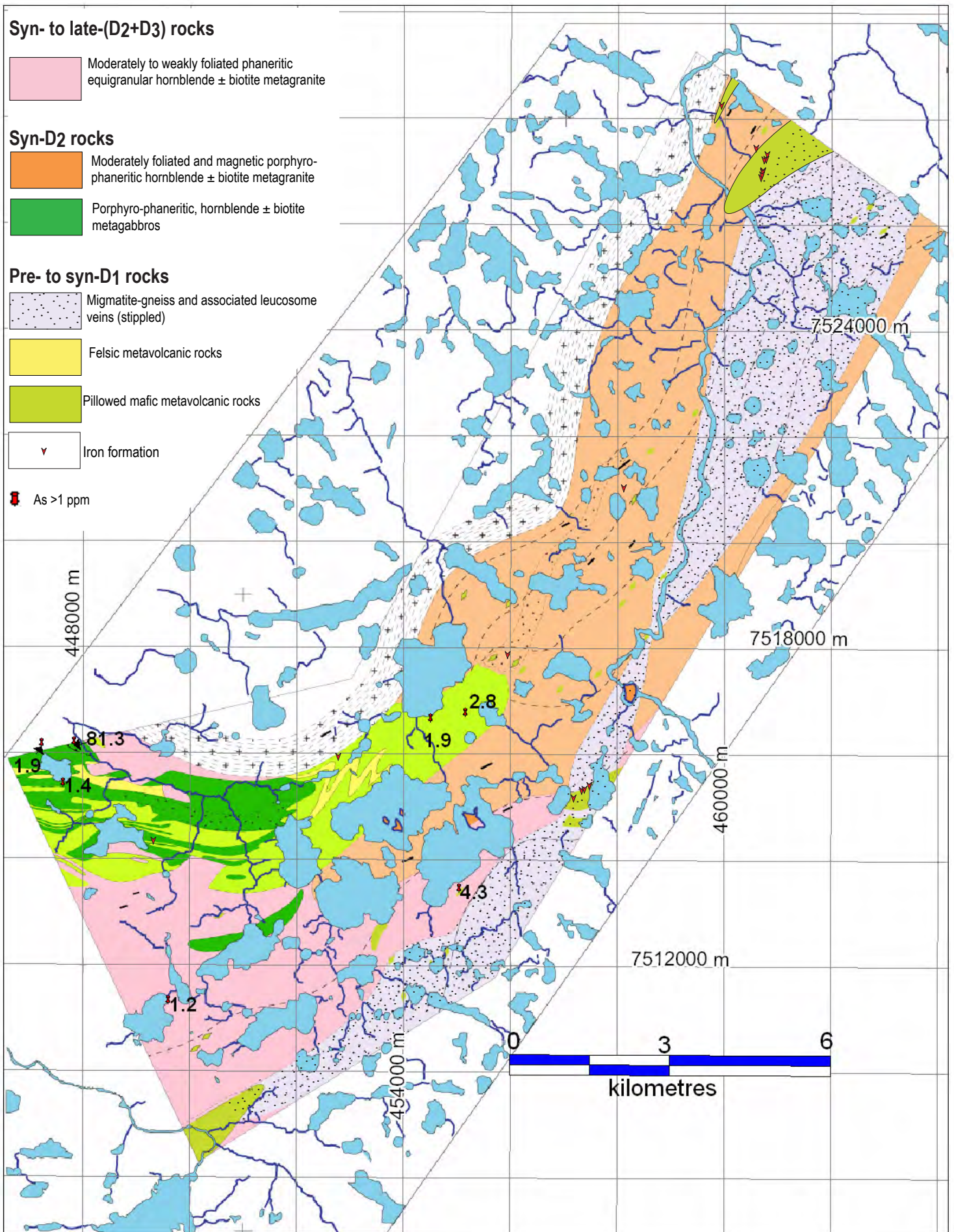




Figure 19.

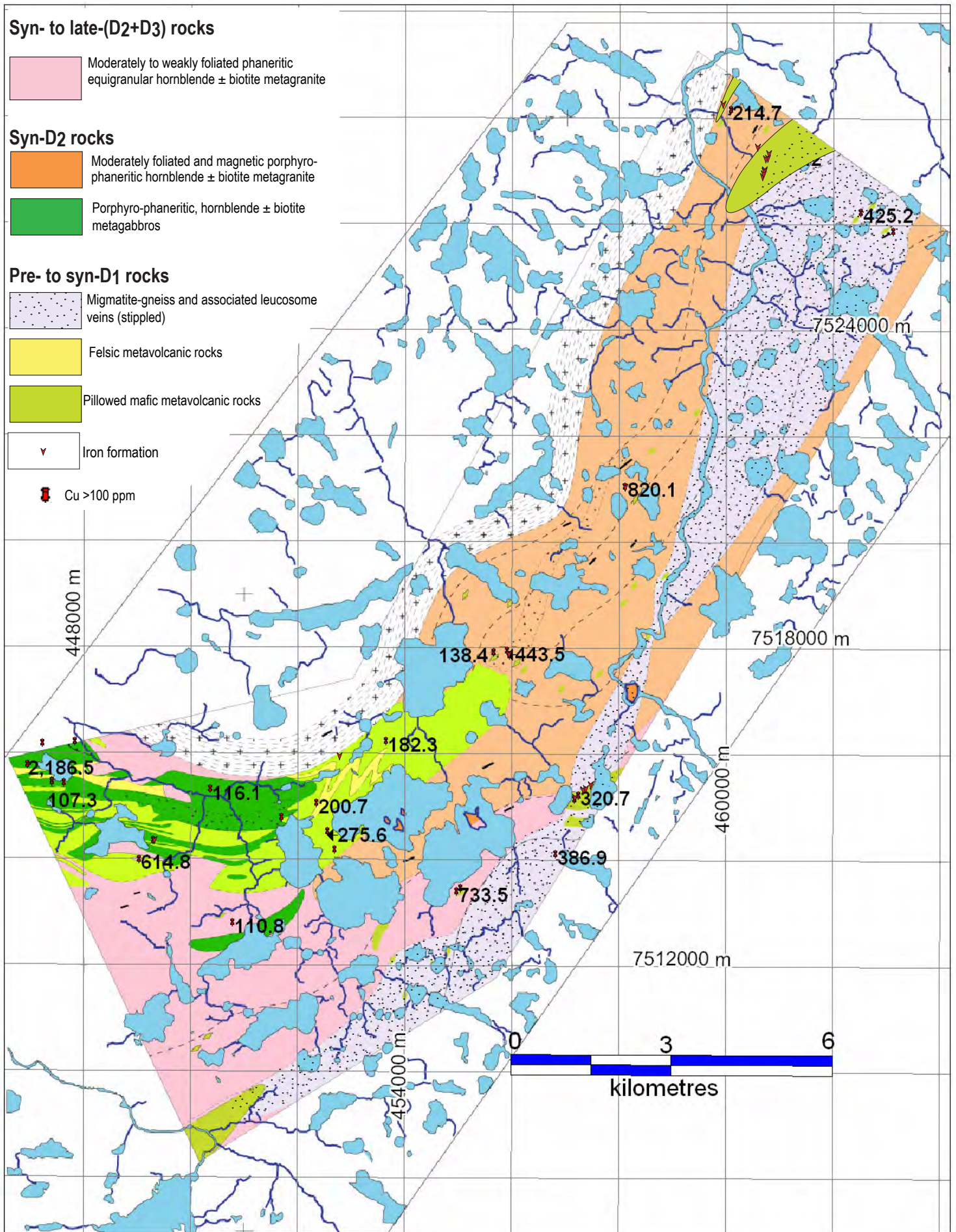
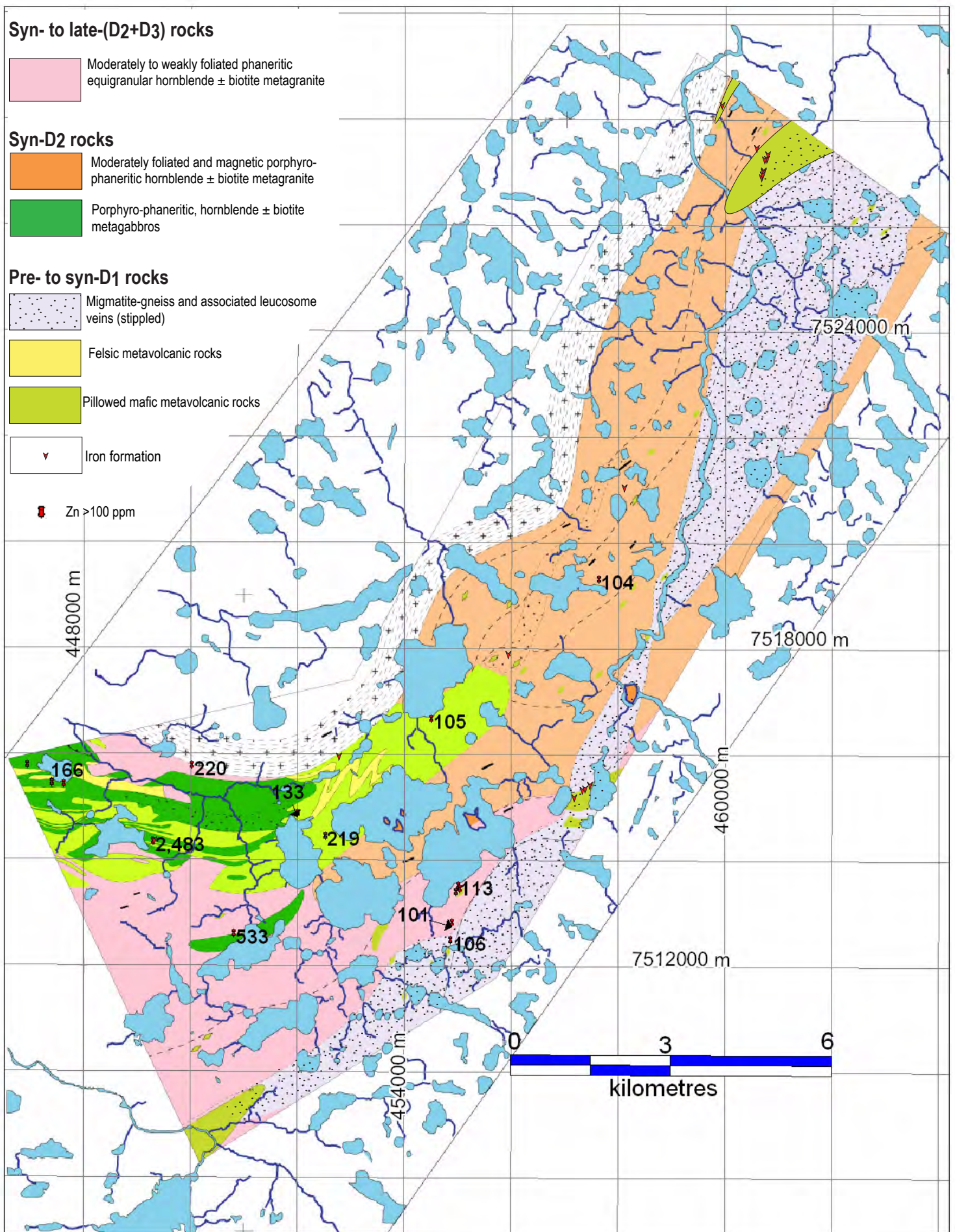




Figure 20.



**Table 1.**

<b>Rock type</b>	<b>n</b>	<b>Magnetic susceptibility</b>
Metagabbros	43	1.68 + 5.88/-1.31
Metagranites	41	1.53 +10.47/-1.30
Metavolcanic rocks	19	1.00 +5.19/-0.85
Dolerites	5	8.64 +15.90/-5.60

**Table 2.**

<b>Mafic metavolcanic rocks</b>			
Deformation	D <sub>1</sub>	D <sub>2</sub>	
Metamorph.	M <sub>1</sub>	M <sub>2</sub>	M <sub>3</sub>
Amphibole	—	—	
Magnetite	—	—	
Plagioclase	—	—	
Biotite	—	—	
Quartz	—	—	—
Chlorite	—	—	—
Zoisite	—	—	—
Titanite	—	—	—
Pyrite	—	—	—
Chalcopyrite	—	—	—
Arsenopyrite	—	—	—
Calcite			—
Sericite			—
Hematite			—

a)

<b>Metapsammitic rocks</b>			
Deformation	D <sub>1</sub>	D <sub>2</sub>	
Metamorph.	M <sub>1</sub>	M <sub>2</sub>	M <sub>3</sub>
Amphibole	—	—	
Magnetite	—	—	
Plagioclase	—	—	
Biotite	—	—	
Titanite	—	—	
Quartz	—	—	—
Chlorite	—	—	—
Zoisite	—	—	—
Pyrite	—	—	—
Chalcopyrite	—	—	—
Arsenopyrite	—	—	—
Sphalerite	—	—	—
Pyrrhotite	—	—	—
Muscovite		—	—
Hematite		—	—

b)

<b>Felsic metavolcanic rocks</b>			
Deformation	D <sub>1</sub>	D <sub>2</sub>	
Metamorph.	M <sub>1</sub>	M <sub>2</sub>	M <sub>3</sub>
Zircon	—	—	
Ilmenite	—	—	
Plagioclase	—	—	
Biotite	—	—	
Quartz	—	—	—
Garnet	—	—	—
Chlorite	—	—	—
Muscovite		—	—
Epidote		—	—
Pyrite	—	—	—
Chalcopyrite	—	—	—
Apatite		—	—

c)

<b>Iron formation</b>			
Deformation	D <sub>1</sub>	D <sub>2</sub>	
Metamorph.	M <sub>1</sub>	M <sub>2</sub>	M <sub>3</sub>
Amphibole	—	—	
Magnetite	—	—	
Quartz	—	—	—
Chlorite	—	—	—
Pyrite	—	—	—
Zoisite	—	—	—
Hematite		—	—

d)

<b>Am ± Bt metagabbros</b>			
Deformation		D <sub>2</sub>	
Metamorph.	M <sub>0</sub>	M <sub>2</sub>	M <sub>3</sub>
Amphibole	—	—	
Magnetite	—	—	
Quartz	—	—	—
Plagioclase	—	—	
Biotite	—	—	
Chlorite	—	—	—
Zoisite	—	—	—
Chalcopyrite	—	—	—
Arsenopyrite	—	—	—
Calcite		—	—
Pyrite		—	—
Sericite		—	—
Hematite		—	—

e)

<b>Bt metagranites</b>			
Deformation		D <sub>2</sub>	
Metamorph.	M <sub>0</sub>	M <sub>2</sub>	M <sub>3</sub>
Orthoclase	—	—	
Magnetite	—	—	
Zircon	—	—	
Plagioclase	—	—	
Biotite	—	—	
Quartz	—	—	—
Titanite	—	—	—
Chlorite	—	—	—
Zoisite	—	—	—
Muscovite		—	—
Microcline		—	—
Pyrite		—	—
Calcite		—	—

f)

<b>Am ± Bt metagranites</b>			
Deformation		D <sub>2</sub>	
Metamorph.	M <sub>0</sub>	M <sub>2</sub>	M <sub>3</sub>
Orthoclase	—	—	
Magnetite	—	—	
Zircon	—	—	
Plagioclase	—	—	
Amphibole	—	—	
Quartz	—	—	—
Zoisite	—	—	—
Chlorite	—	—	—
Microcline		—	—
Biotite		—	—
Titanite		—	—
Pyrite		—	—
Chalcopyrite		—	—
Sericite		—	—
Calcite		—	—
Apatite		—	—

g)

<b>Dolerites</b>		
Deformation		
Metamorph.	M <sub>0</sub>	M <sub>3</sub>
Amphibole	—	
Magnetite	—	
Plagioclase	—	
Chlorite	—	—
Quartz	—	—
Zoisite	—	—
Sericite	—	—
Pyrite	—	—
Chalcopyrite	—	—
Arsenopyrite	—	—

h)

**Table 3.**

<b>Mineral (vol.%)</b> <b>Rock unit</b>	<b>Am</b>	<b>Bt</b>	<b>Grt</b>	<b>Chl</b>	<b>Pl</b>	<b>Qtz</b>	<b>Or</b>	<b>Mc</b>	<b>Ttn</b>	<b>Zo</b>	<b>Ms</b>	<b>Mag</b>
Mafic metavolcanic rocks	20-35	1-10	-	10-15	20-25	8-25	-	-	<1	1-20	<1	<1
Felsic metavolcanic rocks	-	8	4	5	15	65	-	-	-	-	2	-
Metapsammite	3	<1	-	15	8	50	-	-	<1	<1	15	7
Iron formation	25	-	-	4	-	40	-	-	-	3	-	25
Migmatitic gneiss	15-25	5-10	-	5-15	35-45	15-20	5-10	-	<1	-	<1	<1-3
Am ± Bt metagabbro	25-50	<1	-	6-50	15-40	14	-	-	-	1-40	<1	<1
Bt metagranite	-	1-20	-	1-8	15-55	15-45	2-30	0-22	<1	<1	1-5	<1
Am ± Bt metagranite	2-6	1-5	-	8-10	25-30	25-30	15-20	-	1-3	1-5	<1	<1
Dolerite	40-60	-	-	2-10	20-25	0-5	-	-	-	<1	<1	10-15
Anorhosite	10-15	-	-	<1	75-85	-	-	-	-	-	<1	1-5

**Table 3 (continued).**

<b>Mineral (vol.%) Rock unit</b>	<b>Zrn</b>	<b>Ep</b>	<b>Cal</b>	<b>Py</b>	<b>Ccp</b>	<b>Apy</b>	<b>Sp</b>	<b>Po</b>	<b>Ap</b>	<b>Hem</b>
Mafic metavolcanic rocks	-	-	<1	<1	<1	<1	-	-	-	<1
Felsic metavolcanic rocks	<1	<1	-	<1	<1	-	-	-	<1	-
Metapsammite	-	-	-	<1	<1	<1	<1	<1	-	-
Iron formation	-	-	-	<1	<1	<1	<1	-	<1	<1
Migmatitic gneiss	<1	<1	-	<1	<1	<1	-	-	<1	<1
Am ± Bt metagabbro	-	-	<1	<1	<1	<1	<1	-	<1	-
Bt metagranite	<1	-	<1-10	<1	-	-	-	-	-	-
Am ± Bt metagranite	-	-	<1	<1	<1	-	-	-	<1	-
Dolerite	-	-	-	<1	<1	<1	-	-	-	-
Anorthosite	-	-	-	<1	<1	<1	-	-	-	-

**Table 4.**

	Metabasalts	Metarhyolites	Metagabbros	Metagranites	Metapsammites	Iron formation	Metadolerites	Quartz veins
SiO <sub>2</sub> %	51.1	72.6	52.2	66.4	59.9	52.4	49.0	78.6
TiO <sub>2</sub>	1.03	0.26	1.23	0.33	0.62	0.13	1.96	0.55
Al <sub>2</sub> O <sub>3</sub>	13.73	13.10	13.41	14.64	14.14	3.75	13.12	5.30
Fe <sub>2</sub> O <sub>3</sub> T	12.62	3.20	14.59	5.08	9.47	33.66	16.37	6.45
MnO	0.20	0.04	0.18	0.06	0.14	0.13	0.24	0.08
MgO	6.09	1.59	4.80	1.80	2.27	1.88	5.13	1.51
CaO	8.89	2.30	6.69	3.36	5.33	3.80	9.22	3.16
Na <sub>2</sub> O	2.69	2.95	2.56	3.77	3.03	0.78	2.45	0.86
K <sub>2</sub> O	1.29	2.02	0.77	2.87	1.56	0.41	0.69	0.61
P <sub>2</sub> O <sub>5</sub>	0.18	0.04	0.13	0.08	0.19	0.15	0.36	0.08
Cr <sub>2</sub> O <sub>3</sub>	0.03	0.00	0.01	0.01	0.01	0.00	0.00	0.01
LOI	1.83	1.75	3.12	1.40	3.04	2.64	1.17	2.66
Total	99.7	99.8	99.7	99.7	99.6	99.8	99.7	99.9
Ni ppm	103	10	159	24	44	31	56	19
Co	38	6	51	13	27	27	49	45
Sc	29	5	30	9	11	4	42	12
V	226	29	271	64	96	26	396	98
Sn	1.7	1.1	1.0	1.0	2.1	2.4	1.0	1.2
W	0.7	0.5	0.4	0.3	0.6	10.0	0.3	4.3
Rb	45	41	22	86	59	10	31	23
Cs	1.9	1.3	0.6	1.5	1.7	0.7	1.0	3.1
Ba	270	540	159	919	410	131	160	173
Sr	346	137	210	352	398	22	244	61
Ga	18	18	18	18	19	8	18	8
Ta	0.5	0.8	0.3	0.3	1.1	0.2	0.6	0.5
Nb	5.8	10.7	5.9	3.8	8.0	2.7	11.3	10.6
Hf	2.7	7.0	3.2	3.2	3.2	1.0	3.8	1.9
Zr	96	230	111	112	122	34	151	71
Y	23	43	31	7	13	8	34	18
Th	3.6	5.1	1.5	6.3	6.3	1.2	2.3	0.9
U	1.3	1.2	0.4	0.8	3.8	0.6	0.5	0.3
La	19.6	21.1	10.7	17.4	21.3	5.2	21.0	7.8
Ce	47.2	47.1	27.3	35.1	46.4	11.1	50.5	19.4
Pr	5.82	5.68	3.66	3.54	5.11	1.31	6.43	2.50
Nd	24.5	23.0	17.1	12.3	19.5	5.2	26.9	10.8
Sm	5.01	5.07	4.23	1.97	3.40	1.08	5.77	2.33
Eu	1.39	0.94	1.27	0.64	1.03	0.50	1.77	0.63
Gd	4.44	5.74	4.87	1.46	2.64	1.08	5.89	2.60
Tb	0.72	1.11	0.88	0.22	0.42	0.19	1.03	0.48
Dy	4.0	6.6	5.2	1.2	2.2	1.1	6.0	2.9
Ho	0.82	1.48	1.13	0.23	0.44	0.24	1.25	0.66
Er	2.33	4.72	3.39	0.66	1.23	0.72	3.57	2.02
Tm	0.35	0.74	0.51	0.10	0.19	0.12	0.53	0.32
Yb	2.23	4.82	3.23	0.64	1.22	0.75	3.36	2.07
Lu	0.34	0.76	0.50	0.10	0.19	0.13	0.52	0.31
Be	0.90	0.75	0.58	0.63	1.21	0.60	0.50	0.63

**Table 5.**

		Metaba- salts	Metarhyo- lites	Metagab- bros	Metagra- nites	Metapsam- mites	Iron formation	Metado- lerites	Quartz veins
Ti	wt. %	0.25	0.10	0.21	0.10	0.17	0.04	0.22	0.12
Al		2.38	1.67	2.75	1.24	1.77	0.53	2.10	1.32
Fe		4.07	1.89	6.63	2.26	4.72	21.06	5.19	3.61
Mn	(ppm)	575.24	278.50	755.07	207.13	433.14	512.00	513.00	388.38
Mg		1.71	0.83	1.81	0.51	0.68	0.42	0.90	0.73
Ca		1.71	0.55	1.89	0.69	1.14	0.90	2.10	1.41
Na		0.19	0.14	0.18	0.17	0.15	0.06	0.31	0.05
K		0.71	0.57	0.25	0.35	0.41	0.15	0.20	0.36
P		0.09	0.02	0.06	0.04	0.08	0.06	0.15	0.03
S		0.33	0.03	0.99	0.23	1.54	2.01	0.12	0.65
Cr	ppm	45	15	54	20	27	21	23	28
Ni		44	7	213	9	36	30	21	18
Co		24	6	43	8	27	27	24	44
Sc		9	2	11	3	3	2	9	5
V		108	17	161	29	48	22	209	66
Cu		74	17	388	101	353	443	146	110
Pb		3	2	2	9	4	3	3	7
Zn		67	30	87	126	875	564	59	75
Bi		0.21	0.05	0.22	0.22	0.71	0.86	0.05	1.83
Cd		0.06	0.05	0.08	0.56	4.02	1.62	0.08	0.16
Te		0.50	0.50	0.46	0.56	0.57	0.50	0.50	0.91
W		0.1	0.1	0.1	0.1	0.2	6.4	0.1	3.6
Mo		0.9	1.1	0.6	1.0	12.9	2.5	0.5	2.1
As		0.4	0.3	0.4	0.8	0.3	0.3	0.3	5.5
Se		0.80	0.41	1.76	0.71	2.17	2.88	0.25	0.94
Sb		0.0	0.1	0.0	0.1	0.1	0.1	0.1	0.1
Ag		0.06	0.05	0.26	0.23	0.36	0.46	0.07	0.45
Au	(ppb)	1.2	0.3	7.5	2.2	1.9	1.6	2.4	5.4
Hg		0.005	0.005	0.002	0.005	0.005	0.005	0.005	0.005
Ba		74	150	59	84	90	16	47	119
Sr		41	24	28	38	62	4	42	14
Tl		0.22	0.06	0.07	0.14	0.14	0.15	0.07	0.13
Ga		7	7	10	5	7	5	8	5
Th		1.9	5.0	0.9	6.0	5.5	1.1	2.0	0.8
U		0.3	0.6	0.1	0.5	3.0	0.4	0.2	0.2
La		12.7	20.5	9.4	15.4	19.9	4.9	18.7	6.5
B		9	10	9	10	10	10	10	10